

# Long-term fluid circulation in extensional faults in the central Catalan Coastal Ranges: P–T constraints from neoformed chlorite and K-white mica

Irene Cantarero · Pierre Lanari · Olivier Vidal ·  
Gemma Alías · Anna Travé · Vinyet Baqués

Received: 25 December 2012 / Accepted: 21 September 2013 / Published online: 8 October 2013  
© Springer-Verlag Berlin Heidelberg 2013

**Abstract** The neoformation of chlorite and K-white mica in fault rocks from two main faults of the central Catalan Coastal Ranges, the Vallès and the Hospital faults, has allowed us to constrain the P–T conditions during fault evolution using thermodynamic modeling. Crystallization of M1 and M2 muscovite and microcline occurred as result of deuteric alteration during the exhumation of the pluton ( $290\text{ °C} > T > 370\text{ °C}$ ) in the Permian. After that, three tectonic events have been distinguished. The first tectonic event, attributed to the Mesozoic rifting, is characterized by precipitation of M3 and M4 phengite together with chlorite and calcite C1 at temperatures between 190 and 310 °C. The second tectonic event attributed to the Paleogene compression has only been identified in the Hospital fault with precipitation of low-temperature calcite C2. The

shortcut produced during inversion of the Vallès fault was probably the responsible for the lack of neoformed minerals within this fault. Finally, the third tectonic event, which is related to the Neogene extension, is characterized in the Vallès fault by a new generation of chlorite, associated with calcite C4 and laumontite, formed at temperatures between 125 and 190 °C in the absence of K-white mica. Differently, the Hospital fault is characterized by the precipitation of calcite C3 during the syn-rift stage at temperatures around 150 °C and by low-temperature fluids precipitating calcites C5, C6 and PC1 during the post-rift stage. During the two extensional events (Mesozoic and Neogene), faults acted as conduits for hot fluids producing anomalous high geothermal gradients (50 °C/km minimum).

---

I. Cantarero (✉) · G. Alías · A. Travé · V. Baqués  
Departament de Geoquímica, Petrologia i Prospecció Geològica,  
Facultat de Geologia, Universitat de Barcelona (UB), Martí i  
Franqués s/n, 08028 Barcelona, Spain  
e-mail: i\_cantarero@ub.edu

G. Alías  
e-mail: galias@ub.edu

A. Travé  
e-mail: atrave@ub.edu

V. Baqués  
e-mail: vbaques@ub.edu

P. Lanari  
Institute of Geology, University of Bern, Baltzstrasse 1 + 3,  
Bern CH-3012, Switzerland  
e-mail: pierre.lanari@geo.unibe.ch

O. Vidal  
ISTerre, Université de Grenoble I, CNRS, 1381 Rue de la  
Piscine, 38041 Grenoble, France  
e-mail: olivier.vidal@ujf-grenoble.fr

**Keywords** Fault rocks · Low-P–low-T estimates ·  
Chlorite-mica multi-equilibrium · Hydrothermalism ·  
Catalan Coastal Ranges

## Introduction

Chemical and isotopic compositions of minerals formed during faulting can record the origin of the fluids and the pressure and temperature (P–T) conditions of deformation regimes, essential parameters to understand fault evolution. Phyllosilicates such as chlorite and K-white mica allow to quantify the P–T conditions as their chemical composition is temperature and pressure dependent. They have been used to constrain P–T equilibrium conditions of crystallization in high-pressure–low-temperature (HP–LT) and low-pressure–low-temperature (LP–LT) metapelites free of minerals index of metamorphism applying thermodynamic approaches (Vidal and Parra 2000; Parra et al. 2002; Árkai

et al. 2003; Vidal et al. 2006; Schwartz et al. 2009; Dubacq et al. 2010; Ganne et al. 2012; Grosch et al. 2012; Lanari et al. 2012 and references therein). Also, the same approach has been successfully used to constrain diagenetic or low-grade metamorphic conditions during fault evolution (Lacroix et al. 2012; Leclère et al. 2012). In fault zones, phyllosilicates can be inherited from the host rock or authigenic. The latter can be produced by fluid–rock interaction or direct precipitation from circulating fluids (Collettini et al. 2009; Buatier et al. 2012a, b). Alteration of primary minerals to produce weak and fine-grained secondary phases due to fluid–rock interaction has been extensively described in fault zones affecting different lithologies (Evans and Chester 1995; Vrolijk and van der Pluijm 1999; Haines and van der Pluijm 2012). Specifically, in granodioritic systems, the most common reactions consist of the breakdown of anhydrous phases to hydrous minerals: hornblende → carbonate minerals + clays (chlorite, smectite); biotite → carbonate minerals + clays (chlorite, smectite); plagioclase → albite, zeolite, illite (Fujimoto et al. 2001; Jefferies et al. 2006). Also, transformation of fragmental illite or muscovite ( $2M_1$ ) from sedimentary, metamorphic or igneous origin, into low-temperature illite ( $1M_d$ ) is a spread and well-known transformation in most of clay gouges (Haines and van der Pluijm 2012). Moreover, in granitic systems, where Mg is present (i.e., biotites), phyllosilicates such as K-white mica, chlorite and kaolinite are predicted to precipitate at low temperature (below 350 °C) due to water interaction in both rock-dominated and water-dominated systems (Wintsch et al. 1995).

The Catalan Coastal Ranges (CCR), located in the NE of Spain, provide the opportunity to study an area with a long-term multiphase tectonism represented by successive compressional and extensional tectonic events from Mesozoic to recent. Some of the Neogene normal faults, which control the current NE–SW horst and graben structure, are the result of the negative inversion of Paleogene thrusts, which, in turn, inverted previous extensional Mesozoic faults (Bartrina et al. 1992; Santanach et al. 2011). The present work is focused on the study of two NE–SW trending faults where deformation is mostly located in the granodioritic footwall. Because of the long activity of these faults, a detailed study has been done in order to identify the time-relative relationships between the different deformation phases and the P–T conditions of mineral crystallization during the evolution of the fault zones.

Pressure conditions were constrained during the CCR evolution by means of sedimentological, structural and fission-track studies (Anadón et al. 1979; Juez-Larré 2003; Gaspar-Escribano et al. 2004; ter Voorde et al. 2007). These studies demonstrate that rocks outcropping

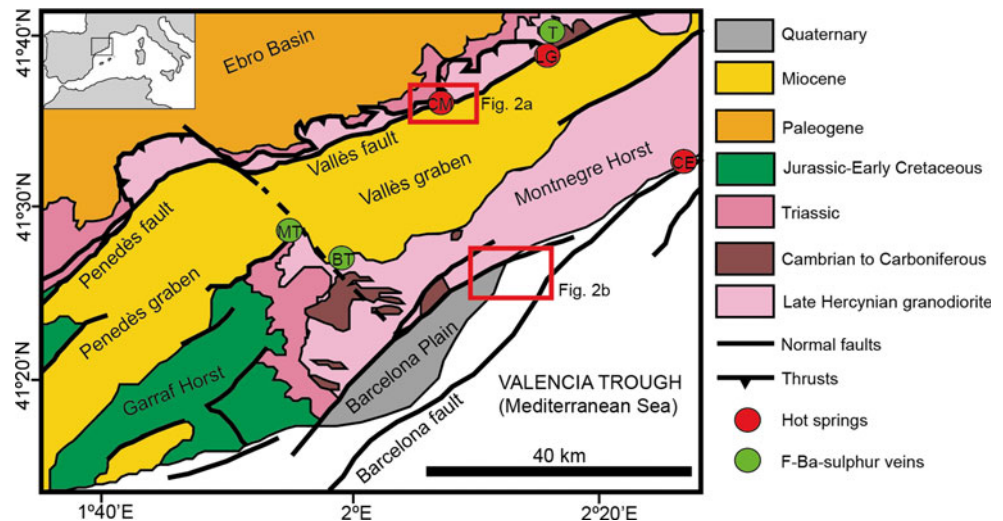
nowadays were at a maximum of 3.6 km depth previous to the Paleogene compression and 2.2 km previous to the Miocene extension, yielding to maximum pressure conditions around 1 and 0.7 kbar, respectively. Temperature conditions were constrained from fluid inclusion data in fluorite-barite veins (Canals and Cardellach 1997; Cardellach et al. 2002; Tritlla and Cardellach 2003; Piqué et al. 2008). In the Central Catalan Coastal Ranges, i.e., in Berta and Rigròs mines, temperatures recorded in the Mesozoic veins range between 80 and 230 °C, whereas Miocene veins formed between 100 and 150 °C (Cardellach et al. 2002; Piqué et al. 2008). Moreover, fission-track data in the CCR (Juez-Larré 2003) provided constrain on the minimum temperature during the Mesozoic and the Neogene corresponding to the closure temperature of apatites and zircons. Temperature was found to drop from  $T > 200$  °C before Mesozoic to the closure temperature of zircon during Mesozoic and down to the closure temperature of apatite (100 °C) during the Miocene. These temperatures mainly occurred in the samples localized close to the graben boundary (Juez-Larré 2003), which is consistent with fluid inclusion data (Piqué et al. 2008).

The above-mentioned data provide a general framework, but a more detailed evolution of the P–T conditions linked to fault activities still remains to be done. In the present study, the combination of petrological observations and multi-equilibrium thermodynamic modeling using the compositions of chlorite and K-white mica allows us to reconstruct the P–T path during evolution of the two faults. The aims of this work are as follows: (1) to characterize the different deformation phases associated with each tectonic event along a major and an intermediate fault (the Vallès and the Hospital faults, respectively) affecting the same granodioritic host rock, (2) to propose a detailed interpretation of the relationships between P–T estimates of mineral crystallization and fault evolution, and (3) to establish the factors that control the different associations of newly formed minerals.

## Geological setting

The Catalan Coastal Ranges (CCR), in the NE of Spain, constitute the north-western edge of the Valencia Trough, separating the thin continental crust of this trough from the thickened crust of the Iberian Peninsula. The opening of the Valencia Trough is related to the southwestward propagation of the Western European rift system and the Burdigalian oceanic accretion associated with the southwestward drift of the Corsica-Sardinia block during the Neogene extensional event (Oligocene-middle Miocene) (Roca et al. 1999). The CCR display a well-developed horst and graben structure limited by listric faults striking

**Fig. 1** Simplified geological map of the central Catalan Coastal Ranges (modified from Santanach et al. 2011). Squares indicate study areas that are enlarged in Fig. 2. T Tagamanent, MT Martorell, BT Berta Mine, CM Caldes de Montbui, LG La Garriga, CE Caldes d'Estrac



NE–SW and NNE–SSW with a detachment level at 12–16 km, acquired during the opening of the Valencia Trough (Fig. 1) (Roca and Guimerà 1992; Gaspar-Escribano et al. 2004). This structure is also segmented by later faults trending NW–SE to NNW–SSE (Fig. 2). The Neogene extensional event is divided into a syn-rift stage (Aquitanian-Late Burdigalian), an early post-rift stage (Langhian-Serravallian) and a late post-rift stage (late Serravallian-Pliocene) (Calvet et al. 1996; Baqués et al. 2013).

This extensional structure is superimposed on Paleogene contractional structures formed during the N–S compression caused by the collision between the Iberian and European plates (Late Cretaceous-late Oligocene), which generated the Catalan Intraplate Chain (Guimerà 1984; Bartrina et al. 1992). The formed thick-skinned thrusts had a certain left-lateral component (Ashauer and Teichmüller 1935; Anadón et al. 1985; Roca 1996).

In its turn, Paleogene thrusts inverted major Mesozoic extensional faults. During the Mesozoic, an extensional process related to the opening of the western Tethys and of the North Atlantic took place (Salas and Casas 1993; Rossi et al. 2001). Two rift stages and two related post-rift stages have been described (Salas et al. 2001). The first rift stage is Late Permian-Early Jurassic in age and was related to the westward propagation of the Tethys and southward propagation of the Arctic-North Atlantic rift. This event was followed by an Early-to-Middle Jurassic post-rift stage characterized by thermal subsidence. The second rift stage lasted from Late Jurassic to Early Cretaceous and was the result of the gradual opening of both the North Atlantic Basin and the Bay of Biscay. A later stage of thermal subsidence was produced during the Late Cretaceous post-rift (late Albian-Maastrichtian).

Nowadays, abundant springs, some of them of hot water (up to 70 °C), occur at the intersection between the NW–SE

to NNW–SSE faults and the main fault system bounding the grabens (Fernández and Banda 1989). These springs are the result of topographically driven meteoric fluids (Carmona et al. 2000; Bitzer et al. 2001) and are preferably located in the igneous basement, which constitutes the footwall of the main fault system, i.e., Caldes de Montbui, La Garriga, and Caldes d'Estrac (Albert et al. 1979). Two hydrothermal events have been described in the Catalan Coastal Ranges from the study of fault-controlled barite-fluorite-sulfur veins (Canals and Cardellach 1997): one during the Mesozoic (at least Jurassic) and the other during the Neogene (lower Miocene) (Cardellach et al. 2002).

This study is focused on the two NE–SW fault zones, formed during the Neogene extension, which delimit the northern boundary of the Vallès Half-graben and the Barcelona Plain: the Vallès and the Hospital faults, respectively (Figs. 1, 2). The Vallès fault is a NE–SW basement fault with dip to the SE that had a normal displacement up to 4 km during the Neogene extension (Roca et al. 1999). The Vallès Half-graben is up to 65 km long and from 3 to 15 km wide, and it is filled by more than 3,000 m of sediment next to the fault (Cabrera 1981; Bartrina et al. 1992; Roca et al. 1999) ranging in age from late Oligocene to present. The Hospital fault is also a NE–SW basement normal fault with dip to the SE which displacement has been estimated in 1–2 km in function of the fault dip and the absence of the rocks of the contact aureole (about 800 m). The Barcelona Plain is a 40-km-long and 2–10-km-wide basin that is mainly filled by Miocene continental-transitional siliciclastic deposits and Quaternary fluvio-deltaic deposits. In both cases, a Paleozoic basement and a Mesozoic cover mainly constitute the footwalls, although Mesozoic rocks have been almost eroded in the Montnegre horst (Fig. 1). The Paleozoic basement is formed by Cambro-Ordovician shales and phyllites, Silurian black shales and phyllites, Devonian carbonates, Carboniferous

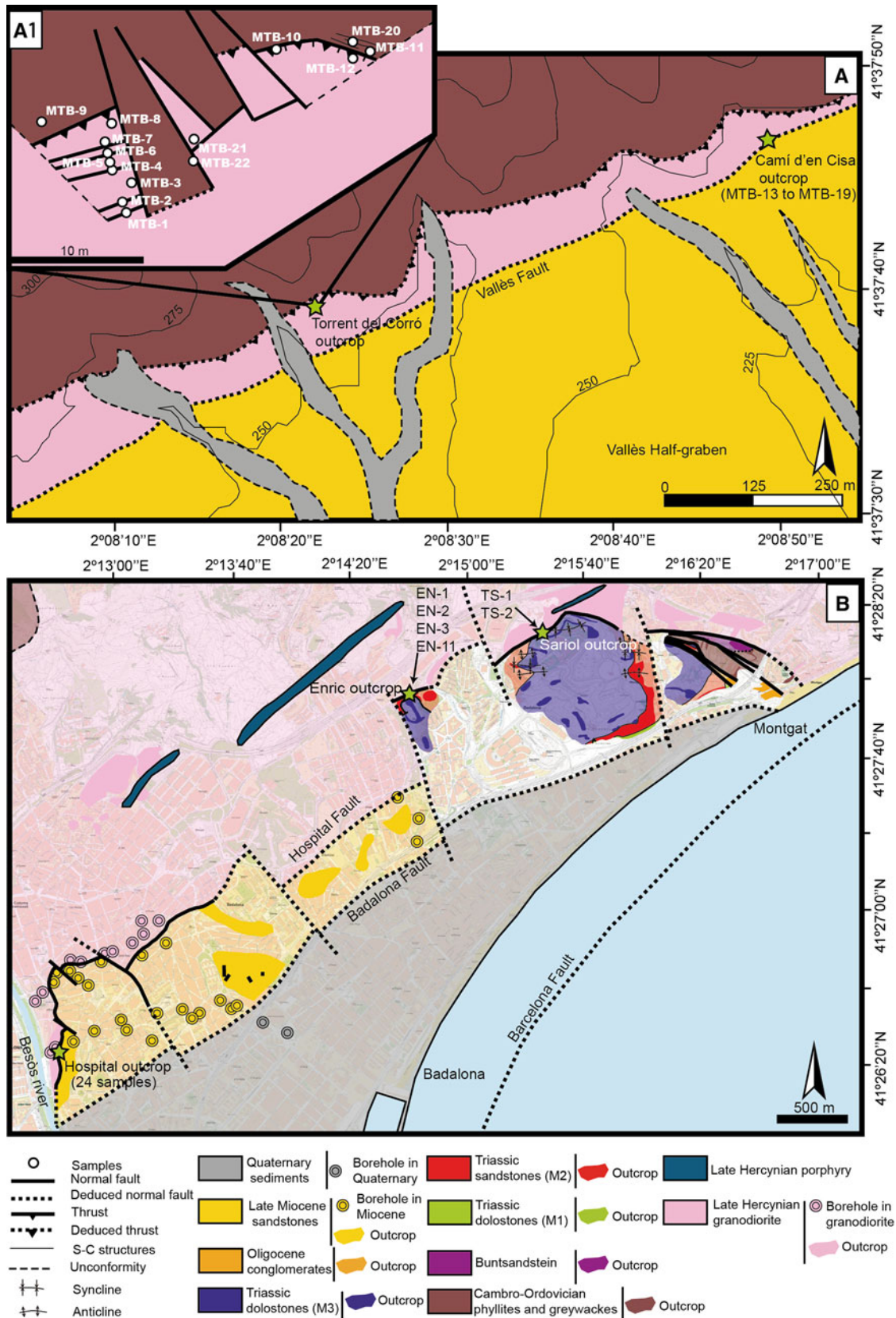


**Fig. 2** Simplified geological maps of the studied areas. **a** Vallès fault in the vicinity of Caldes de Montbui village and outcrop situation. **A1** Enlarged area of the Torrent del Corró outcrop with sample location. **b** Northern sector of Barcelona Plain

Culm facies and late Hercynian leucogranites, tonalites and granodiorites (Julivert and Durán 1990). According to Gilbarguchi and Julivert (1988), the granodiorite was emplaced at 1.5 kbar and 700 °C in the Montnegre Horst close to the Barcelona Plain in function of the mineral assemblages produced in the inner contact metamorphic aureole. It shows granular texture and grain size is mostly about 2–3 mm although some feldspars are around 5 mm. It is constituted by quartz, potassic feldspar, plagioclase and biotite (<5 %). The studied faults mainly affect the late Hercynian granodiorite, which has recorded all the described tectonic events overprinting the Hercynian deformation. As mentioned above, the P–T conditions in the area during these tectonic events have been estimated by fission-track studies (Juez-Larré 2003) and fluid inclusion data in fluorite-barite veins (Canals and Cardellach 1997; Cardellach et al. 2002), establishing 1 kbar–80 to 230 °C for the Mesozoic and 0.7 kbar–100 to 150 °C for the Neogene.

## Methodology

### Petrology and geochemistry

Thirty samples from the Hospital fault, twenty-two from the Vallès fault and two samples of the unaltered granodiorite obtained from boreholes have been studied. Thin sections were examined under optical and cathodoluminescence microscopes. A Technosyn Cold Cathodoluminescence Model 8200 MkII operating at 16–19 kV and 350 µA gun current was used. Selected thin sections were also examined under ESEM Quanta 200 FEI, XTE 325/D8395 scanning electronic microscope combined with EDS spectroscopy for mineral identification.

X-ray diffraction of bulk rock and oriented aggregates have been performed with a Bragg–Brentano PAnalytical X'Pert PRO MPD alpha 1 operating at 1.5406 Å, 45 kV and 40 mA.

After the petrographic study, carbon-coated polished thin sections were analyzed for elemental composition of carbonate cements, chlorites and K-white mica with a CAMECA SX-50 electron probe microanalyzer (EPMA). It operated at 15 nA of beam intensity, 20 kV of acceleration voltage and a beam diameter of 10 µm. The detection limits were 428 ppm for Na, 275 ppm for Mg, 272 ppm for Al, 288 ppm for Si, 263 ppm for K, 260 ppm for Ca, 290 ppm for Ti, 672 ppm for Mn, 647 ppm for Fe for silicates. The precision of major elements is 0.64 % (at 2σ level).

Microsamples of the calcite cements were powdered with a microdrill for carbon and oxygen isotopes. Samples

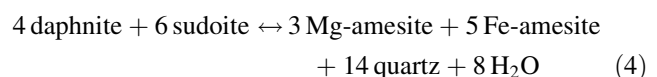
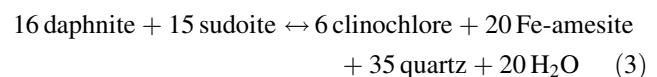
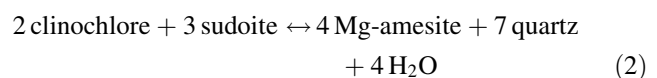
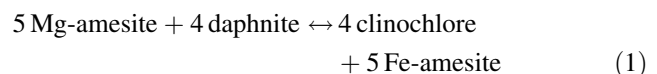
were reacted with 100 % phosphoric acid at 70 °C for 2 min in an automated Kiel Carbonate Device attached to a Thermal Ionization Mass Spectrometer Thermo Electron (Finnigan) MAT-252. The results are expressed in δ ‰ VPDB standard. Standard deviation is ±0.02 ‰ for δ<sup>13</sup>C and ±0.05 ‰ for δ<sup>18</sup>O.

### Thermobarometric methods

Chlorite and K-white mica minerals are good candidates for thermobarometric estimates because they present several chemical substitutions (simple and coupled) controlled by the equilibrium conditions (P, T, pH, fO<sub>2</sub>...) that can be modeled using a set of different end-members (Vidal et al. 2001, 2005, 2006; Parra et al. 2002; Dubacq et al. 2010). Three main substitutions occur in chlorite (FeMg<sub>1</sub>, Tschermak and di/trioctahedral substitutions) that can be modeled using the following set of five end-members (e.g., Vidal et al. 2005): Mg-amesite (Si<sub>2</sub>Al<sub>4</sub>Mg<sub>4</sub>O<sub>10</sub>(OH)<sub>8</sub>), Fe-amesite (Si<sub>2</sub>Al<sub>4</sub>Fe<sub>4</sub>O<sub>10</sub>(OH)<sub>8</sub>), daphnite (Si<sub>3</sub>Al<sub>2</sub>Fe<sub>5</sub>O<sub>10</sub>(OH)<sub>8</sub>), clinochlore (Si<sub>3</sub>Al<sub>2</sub>Mg<sub>5</sub>O<sub>10</sub>(OH)<sub>8</sub>), and sudoite (Si<sub>3</sub>Al<sub>4</sub>Mg<sub>2</sub>□<sub>1</sub>O<sub>10</sub>(OH)<sub>8</sub>). In K-white mica, three additional substitutions occur (NaK<sub>1</sub>, □-(H<sub>2</sub>O)<sub>1</sub> and pyrophyllitic substitutions) and can be modeled using the following set of seven end-members (e.g., Dubacq et al. 2010): muscovite (Si<sub>3</sub>Al<sub>3</sub>□<sub>1</sub>K<sub>1</sub>O<sub>10</sub>(OH)<sub>2</sub>), Fe-celadonite (Si<sub>4</sub>Al<sub>1</sub>Fe<sub>1</sub>□<sub>1</sub>K<sub>1</sub>O<sub>10</sub>(OH)<sub>2</sub>), Mg-celadonite (Si<sub>4</sub>Al<sub>1</sub>Mg<sub>1</sub>□<sub>1</sub>K<sub>1</sub>O<sub>10</sub>(OH)<sub>2</sub>), phlogopite (Si<sub>3</sub>Al<sub>1</sub>Mg<sub>3</sub>K<sub>1</sub>O<sub>10</sub>(OH)<sub>2</sub>), pyrophyllite (Si<sub>4</sub>Al<sub>2</sub>□<sub>2</sub>O<sub>10</sub>(OH)<sub>2</sub>), pyrophyllite-1H<sub>2</sub>O (Si<sub>4</sub>Al<sub>2</sub>□<sub>1</sub>(H<sub>2</sub>O)<sub>1</sub>O<sub>10</sub>(OH)<sub>2</sub>), and paragonite (Si<sub>3</sub>Al<sub>3</sub>□<sub>1</sub>Na<sub>1</sub>O<sub>10</sub>(OH)<sub>2</sub>).

### Chlorite-quartz-water thermometry

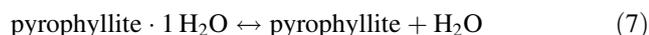
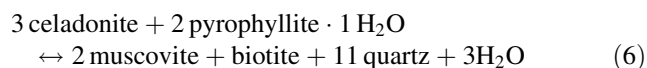
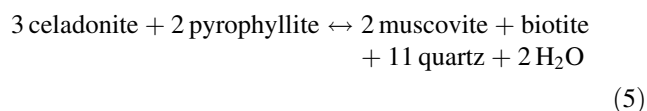
Chlorite shows an increase in Al<sup>IV</sup> and a decrease in vacancy contents with increasing temperature (e.g., Cathelineau and Nieva 1985 and Vidal et al. 2001). The multi-equilibrium approach of Vidal et al. (2005, 2006) proposes a simultaneous estimate of Fe<sup>3+</sup> content in chlorite and equilibrium temperature by the convergence of the following equilibria at a given pressure:



The position of these equilibria, (1) to (4), depends on the activities of the chlorite end-members, quartz and water. In this work, temperatures and  $X_{\text{Fe}^{3+}}$  of chlorite were estimated at 1 kbar, which is the maximum pressure according to the regional geology, and with water activity equal to 1. Following the Vidal et al. (2005, 2006) approach, the convergence is achieved with the minimum  $\text{Fe}^{3+}$  proportion, and it was considered to be achieved when the temperature difference between the four equilibria was less than 30 °C (Lanari et al. 2012 and references therein).

#### *Mica-quartz-water thermobarometry*

The Si content of K-white mica increases with pressure by Tschermak substitution (Massone and Schreyer 1989). At low temperature, the pyrophyllitic substitution also controls the Si and interlayer contents (e.g., Agard et al. 2001). The mica-quartz-water equilibrium used in this study models the variation of composition with respect to temperature and pressure, taking into account mica hydration of vacancies (Dubacq et al. 2010; Vidal et al. 2010). For a mica in chemical equilibrium with quartz and water, these three equilibria can be written as follows:



The convergence of these equilibria at various P–T conditions is achieved by varying the  $X_{\text{H}_2\text{O}_{\text{interlayer}}}$  content (i.e., pyrophyllite·1H<sub>2</sub>O proportion). A mica-quartz-H<sub>2</sub>O equilibrium line is then drawn, along which the hydration state varies (Dubacq et al. 2010). The pressure conditions were then estimated at the temperature obtained from the chlorite-quartz-water equilibria (Lanari et al. 2012). Due to the high proportion of  $\text{Fe}^{3+}$  in chlorite estimated with the chlorite-quartz-water thermometer (see Table 3),  $\text{Fe}^{3+}$  in mica was assumed to be of 50 %.

#### *Chlorite-mica-quartz-water multi-equilibrium approach*

After the application of the previous thermometer and barometer, the equilibrium of chlorite and K-white mica was checked through a full chlorite-mica multi-equilibrium approach involving  $X_{\text{Fe}^{3+}}$  in both chlorite and mica and  $X_{\text{H}_2\text{O}_{\text{interlayer}}}$  in mica. P–T equilibrium conditions of chlorite-mica-quartz-water assemblage were calculated from the convergence of 159 equilibria obtained from the previous mentioned chlorite and mica end-members. Only

those equilibria showing a good convergence were selected. This selection was based on an arbitrary limit for the sum of the Gibbs free energy of a selected set of reactions ( $\Delta rG$ ) at the calculated P and T.

#### **Outcrop description and structural analysis**

The Vallès fault is a major NE–SW normal fault that juxtaposes the Miocene deposits that fill the Vallès Half-graben against the late Hercynian granodiorite (Fig. 2a). In its turn, the granodiorite thrusts in a northwestern direction over the Cambro-Ordovician rocks. The Vallès fault generates a fault zone about 60 m thick localized in the granodioritic footwall. Two outcrops separated 600 m have been selected in the footwall of the Vallès fault according to their structural position: the Torrent del Corró (TCO) and Camí d'En Cisa (CCO) outcrops. The Torrent del Corró outcrop is located at 50 m to the north from the main Neogene Vallès fault and the granodiorite exhibits an intense fracturation. The outcrop shows a step-like geometry, with blocks up to 2 m long descending from NW to SE, caused by normal faults with a NE–SW strike and high dip to the SE. Later NW–SE dextral strike-slip faults offset both normal and thrust faults (Fig. 2a1). On the other hand, the Camí d'En Cisa outcrop is located at the tectonic contact between the granodiorite and the Miocene rocks. The granodiorite is affected by a subordinated conjugated fault system parallel to the main Vallès fault. At the vicinity of the main fault, fracturation is more intense and generates sigmoids that are consistent with a certain left-lateral displacement.

The Hospital fault is a NE–SW fault zone with increasing dip to the NE from 29 to 63°SE. This fault separates the granodiorite (footwall) from the Triassic rocks in the NE and Miocene rocks in the SW (hanging-wall) (Fig. 2b). This fault is offset in different segments, from 200 to 1,500 m long, by NW–SE faults. Three outcrops have been studied: the Hospital, Enric and Sariol outcrops. Each outcrop is located in one of the segments that constitute the Hospital fault and shows the tectonic contact with the Middle Triassic rocks (Fig. 2b). The different outcrops show the strong lateral variations of the fault architecture, which have been linked with the different stages of fault activity and fault growth from Mesozoic to Recent (Cantarero et al. 2013). In the Hospital and Sariol outcrops, the granodiorite is in tectonic contact with the Middle Triassic clays and sandstones and deformation is localized in the footwall whereas in the Sariol outcrop the granodiorite is in tectonic contact with the Middle Triassic dolostones and deformation is produced in both footwall and hangingwall. In the Hospital outcrop, the Hospital fault is represented by a core zone about 70 cm wide with well-

defined sharp boundaries formed by cataclastic material. In the Enric outcrop, the Hospital fault is formed by a 2-m-thick damage zone with irregular boundaries represented by a cohesive breccia and a 20-cm-thick fault core with well-defined sharp boundaries filled by a semi-cohesive gouge. Finally, in the Sariol outcrop, the Hospital fault is formed by a 1 to 3-m-thick fault core constituted by breccias and cataclasites.

The study of crosscutting relationships of the different sets of fractures at outcrop and thin section scales has allowed us to define six deformation phases (Fig. 3). The first deformation phase ( $D_1$ ) is formed by type 1 fractures. They consist of NE–SW striking normal faults that dip from 30 to 60° to the SE and NW. The second deformation phase ( $D_2$ ) is defined by type 2 faults, which are NE–SW reverse faults with a limited left-lateral motion and a dip

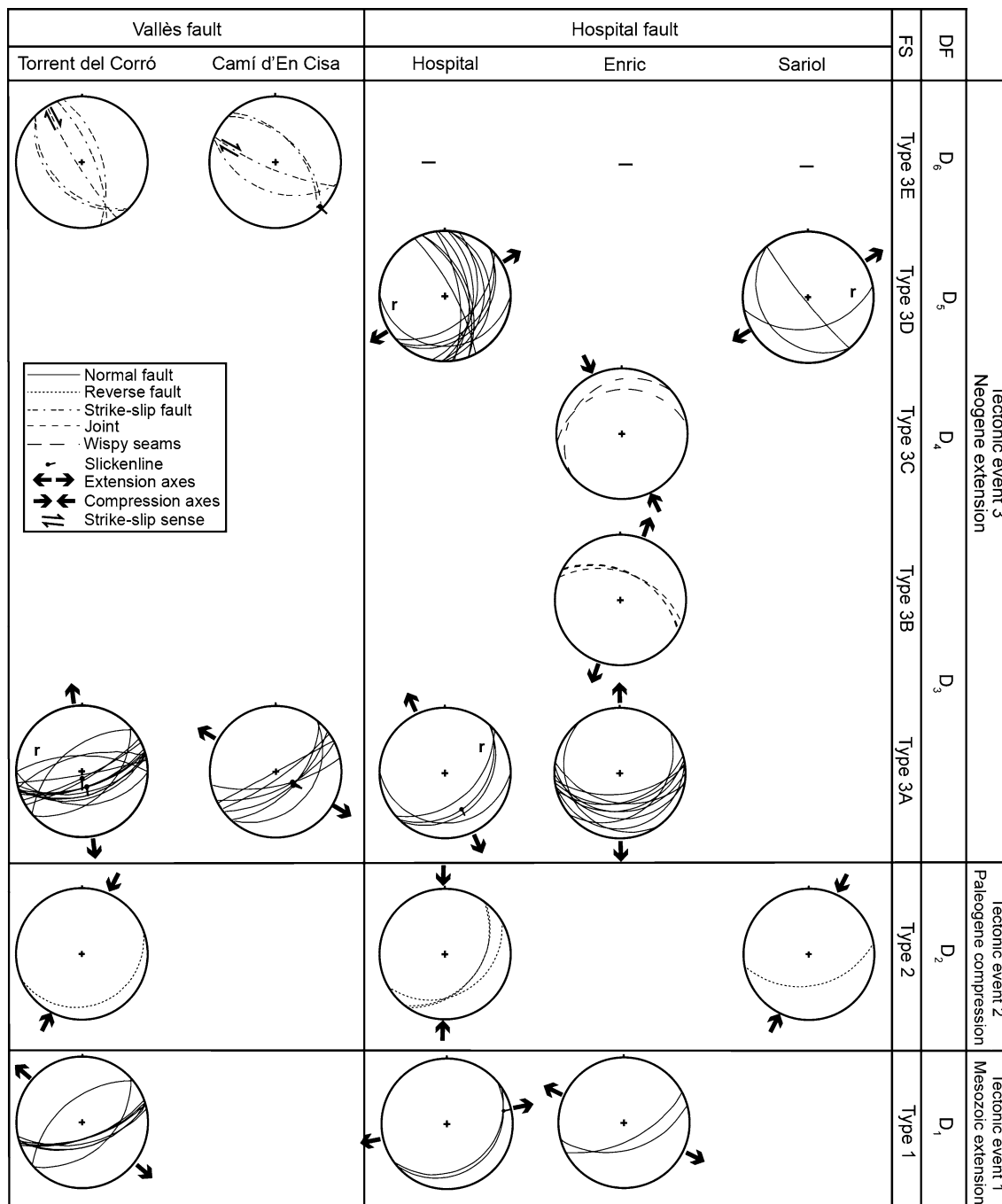


**Fig. 3** Stereoplots in Schmidt lower hemisphere projections of the different generations of fractures according to crosscutting relationships. FS fracture set, DF deformation phase, r reactivated fracture

from 22 to 44°SE. The third deformation phase ( $D_3$ ) is related to type 3A and 3B fractures. Type 3A fractures are E–W to NE–SW striking normal faults with a variable dip (from 15 to 90°) mostly to the E–SE and show dip-slip slickenlines. Some of these faults are the reactivation of type 1 faults. Type 3B fractures are tension veins of NW–SE trend and dip 55°NE. The fourth deformation phase ( $D_4$ ) is characterized by type 3C wispy seams that have NE–SW orientation and low dip to the NW. Type 3B and 3C structures have been only identified in the Enric outcrop. Deformation phase  $D_5$  is represented by type 3D fractures, which consist of normal faults of mainly N–S direction dipping from 30 to 80°E and barely to the SW and NE–SW normal faults that are the reactivation of previous 2 and 3A faults (Fig. 3). Finally, the last deformation phase ( $D_6$ ) is represented by type 3E dextral strike-slip faults trending NW–SE and dipping 50–65° to the northeast and southwest. In the Hospital fault, type 3E faults have been deduced by cartographical criteria.

#### Fluid/fault evolution: petrology of fault rocks and cements

Deformation in the Vallès and Hospital faults generates cohesive brittle fault rocks, from breccias to ultracataclites, and gouges in the granodiorite constituting the footwall. Petrological and geochemical results show the presence of several newly formed minerals such as calcite, laumontite, iron oxides, white mica and chlorite and also some mineral replacements (orthoclase by microcline, biotite by chlorite and coarse-grained muscovite by fine-grained K-white mica). All these minerals vary along fault zones and may differ between faults (Fig. 4a) and show different mineral associations depending on the deformation phase (Fig. 4b).

##### The Vallès fault

From the six described deformation phases, four have been identified in the Vallès fault (Fig. 3). Crystallization of coarse, between 0.2 and 1.1 mm long, idiomorphic K-white mica associated with microcline neoformation with tartan-like twin, occurred previously to these phases. Pseudotachylyte veins with corroded quartz clasts and a very fine-grained matrix (Fig. 5a) clearly postdates the K-white mica. However, it is difficult to establish to which tectonic event these pseudotachylytes are related to due to their later reworking and the lack of preferential orientations. The first deformation phase ( $D_1$ ) consists of type 1 normal faults, characterized by development of cataclases and ultracataclases and microfractures, where small K-white mica grains (15 and 90  $\mu\text{m}$  in size) and ameboid chlorite

precipitated. Also, during this phase, calcite C1 precipitated in nodules. Calcite C1 is made of dull to bright orange crystals, usually twinned, with  $\delta^{18}\text{O}$  values about  $-15\text{‰}$  VPDB and  $\delta^{13}\text{C}$  about  $-6.5\text{‰}$  VPDB (Table 1). The first deformation phase and the previous stages have been only identified in the Torrent del Corró outcrop. The second deformation phase ( $D_2$ ), characterized by reverse faults, developed a wide blue gouge band at basin scale. In the studied outcrops, however, evidences of this deformation phase have been uniquely observed in the Torrent del Corró outcrop represented by narrow gouge bands and stylolites. The third deformation phase ( $D_3$ ) is characterized by successive cataclase development along 3A normal faults and by the alternating precipitation of laumontite and calcite C4 in these fractures and in vug porosity (Fig. 5a–c). Coevally, irregular and ameboid chlorite crystals precipitated along reactivated type 1 and new 3A normal faults. The first generation of laumontite L1 is made of translucent, anhedral and up to 50  $\mu\text{m}$  in size crystals (Fig. 5a). L1 precipitation was followed by cementation of calcite C4, which precipitated in fractures and formed the slickenlines observed in faults 3A. Some of these fractures reopen stylolites formed during  $D_2$  (Fig. 5b). Calcite C4 is formed by bright and dull orange zoned twinned calcite crystals with  $\delta^{18}\text{O}$  values about  $-23\text{‰}$  VPDB and  $\delta^{13}\text{C}$  values about  $-7.5\text{‰}$  VPDB (Table 1). Finally, the second generation of laumontite L2 precipitated and replaced calcite C4 at the wall of some fractures (Fig. 5c). Laumontite crystals are tabular, brownish under plane light and from cryptocrystalline to 70  $\mu\text{m}$  in size (Fig. 5c, d). In this third deformation phase, chlorite, laumontite L1 and calcite C4 are mainly formed in the Torrent del Corró outcrop, whereas laumontite L2 is the main neoformed mineral cementing most of the fractures and breccias in the Camí d'en Cisa outcrop (Fig. 5d). The strike-slip faults  $D_6$  crosscutting previous fault rocks configure the fourth deformation phase identified in this fault zone.

The different neoformed minerals within the two outcrops are the responsible of the different color of fault zones, green in the Torrent del Corró outcrop, due to chlorite crystallization, and white in the Camí d'en Cisa outcrop.

##### The Hospital fault

Fault-related cements of the three studied outcrops (Hospital, Enric and Sariol) are described in detail in Cantarero et al. (2013) but a brief description is provided below.

In the Hospital outcrop, four deformation phases have been identified. During the first deformation phase ( $D_1$ ), a type 1 fault generated a green cataclastic core zone in the contact between the granodiorite and the Middle Triassic

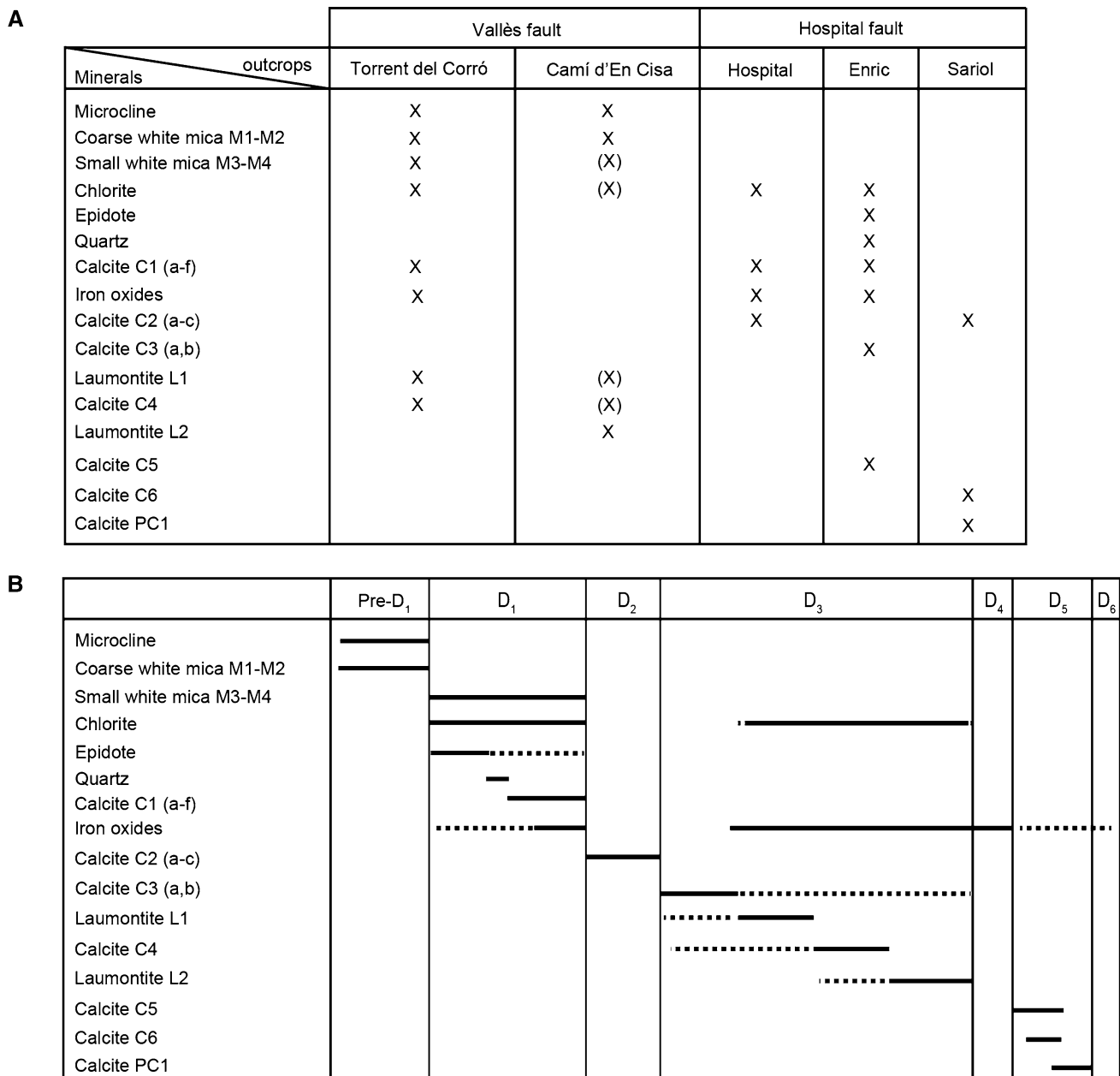


**Fig. 4** Neofomed minerals. **a** Neofomed minerals constituting fault rocks in the outcrops of the Vallès fault and Hospital fault. X marks the outcrops where the mineral is present and (X) when it is almost

inexistent. **b** Temporal relationships between them. With continuous or dotted lines is marked the degree of certainty of a mineral phase

clays and sandstones. This core zone, developed in a zone where previously quartz geodes had formed, is the result of two successive reactivations that produced a dilatant random breccia and a consequent cataclasite. The dilatant random breccia was formed and cemented by five calcite cements, from C1a to C1e, with alternating bright to dull orange luminescence (Fig. 5e, f). Due to the small size of these calcite crystals (up to 1 mm) only a bulk isotopic composition could be obtained. The  $\delta^{18}\text{O}$  values range between  $-15.6$  and  $-15$  ‰ vPDB and the  $\delta^{13}\text{C}$  between

$-6.5$  and  $-6.3$  ‰ vPDB. This dilatant breccia was further deformed as a slightly foliated cataclasite cemented by calcite cement C1f, iron oxides and chlorites. Calcite C1f has  $\delta^{18}\text{O}$  values between  $-16.4$  and  $-16.2$  ‰ vPDB and  $\delta^{13}\text{C}$  values between  $-6.2$  and  $-5.9$  ‰ vPDB (Table 1). The second deformation phase ( $D_2$ ) is represented by reverse faults involving Mesozoic, Ordovician and Silurian rocks that develop decimetric-scale duplexes formed by breccias. During this phase, vug porosity formed within the dilatant breccia ( $D_1$ ) and joints within the Triassic

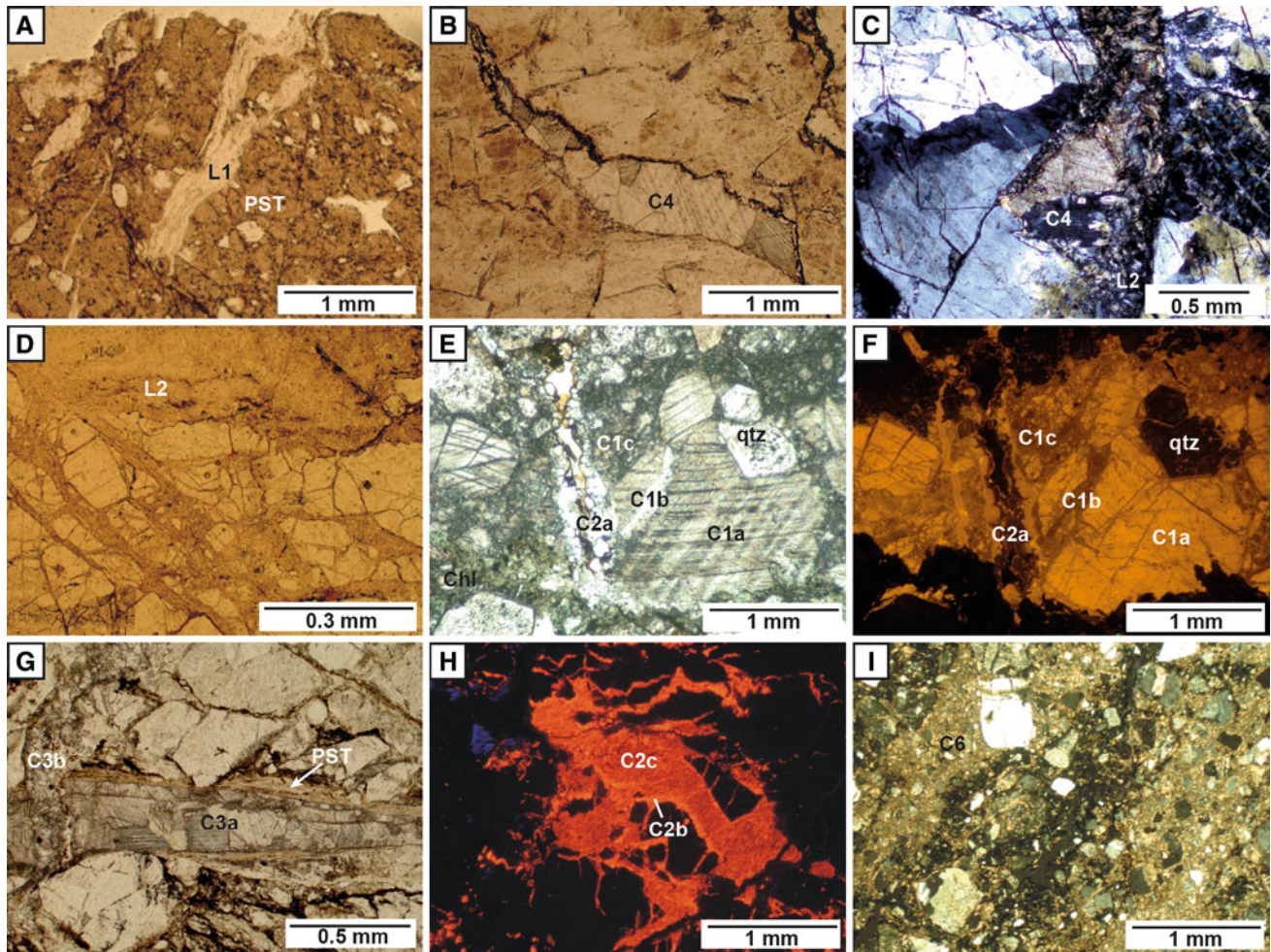


**Fig. 5** Representative microphotographs of the cements identified in the Vallès and Hospital faults. **a** Pseudotachylyte affected by later 3A fractures cemented by laumontite L1. Plane polarized light. **b** Calcite C4 vein resulting from the reopening of a previous stylolite. Plane polarized light. **c** Replacement of calcite C4 by laumontite L2 at the fracture wall. Cross polarized light. **d** Dilatant breccia formed in type 3A faults of the Camí d'en Cisa outcrop cemented by the brownish laumontite L2. Plane polarized light. **e, f** Crosscutting relationships between quartz, several generations of calcite C1 and calcite C2a in

the Hospital fault. Plane polarized light and cathodoluminescence images, respectively. **g** Type 3A fractures formed by pseudotachylyte and later calcite C3a. Both fillings are in turn crosscut by type 3B fractures cemented by calcite C3b. Plane polarized light. **h** Dilatant breccia of the Sariol outcrop cemented by the generations of calcite C2b and C2c. Cathodoluminescence image. **i** Calcite C6 cementing the last cataclasis generation of the Hospital fault. Cross polarized light

sandstones of the hangingwall were cemented by cement C2a. This cement is constituted by anhedral calcite crystals with a zoned orange and brown luminescence. The  $\delta^{18}\text{O}$  values of C2a range between  $-5.5$  and  $-4.6$  ‰ vPDB and the  $\delta^{13}\text{C}$  between  $-7.2$  and  $-6.5$  ‰ vPDB (Table 1). The third deformation phase,  $D_3$ , generates normal faults where fault rocks or cements have not been observed. The fourth deformation phase recorded in the Hospital outcrop corresponds to  $D_5$ , which generates minor normal faults within the Miocene rocks without a fault core.

In the Enric outcrop, the first deformation phase ( $D_1$ ) produced the development of a random breccias, formed by clasts of granodiorite and dynamically recrystallized quartz-feldspathic rocks, with chlorite and epidote

precipitation in the fractures. Later, multiepisodic pull-aparts developed in type 1 microfaults were cemented by calcite C1. Calcite C1 has a bright orange luminescence and  $\delta^{18}\text{O}$  values about  $-15.1$  ‰ vPDB and  $\delta^{13}\text{C}$  values about  $-6.9$  ‰ vPDB. The next deformation phase recognized in this outcrop is  $D_3$  (Fig. 3), which is characterized by the development of pseudotachylytes in type 3A normal faults. This generation of fractures was later reactivated and cemented by calcite C3a forming crack-seals (Fig. 5g). Simultaneously, a gouge was formed. Consequent type 3B fractures were produced and cemented by calcite C3b (Fig. 5g). Both calcites C3 are formed by bright orange calcite crystals that have  $\delta^{18}\text{O}$  values between  $-20$  and  $-18$  ‰ vPDB and  $\delta^{13}\text{C}$  values about  $-6$  ‰ vPDB

**Table 1** Isotopic composition ( $\delta^{18}\text{O}$  and  $\delta^{13}\text{C}$  ‰VPDB) of calcite cements of the Vallès and Hospital faults in function of the outcrop and the different deformation phases

Deformation phase	Cement generation	$\delta^{18}\text{O}$ ‰ VPDB	$\delta^{13}\text{C}$ ‰ VPDB	Outcrop
$D_1$	C1a	−15.6	−6.5	Hospital
		−15.6	−6.5	Hospital
		−15.0	−6.3	Hospital
	C1f	−16.2	−5.9	Hospital
		−16.4	−6.2	Hospital
	C1	−15.1	−6.9	Enric
		−15.0	−7.8	Torrent del Corró
$D_2$	C2a	−4.9	−7.1	Hospital
		−4.6	−6.5	Hospital
		−5.5	−7.0	Hospital
	C2b-c	−5.8	−7.2	Sariol
$D_3$	C3a	−20.5	−6.2	Enric
		−20.0	−6.2	Enric
		−20.3	−6.2	Enric
		−20.8	−6.1	Enric
		−20.3	−6.2	Enric
		−19.6	−6.2	Enric
		−18.4	−6.1	Enric
	C3b	−22.2	−7.7	Torrent del Corró
		−20.9	−8.0	Torrent del Corró
		−22.8	−7.2	Torrent del Corró
$D_5$	C5	−5.8	−7.7	Enric
		−2.6	−7.6	Sariol
	C6	−2.9	−7.6	Sariol
		−2.6	−7.7	Sariol
		−1.9	−7.7	Sariol

(Table 1). During deformation phase  $D_4$ , undulose and discontinuous type 3C wispy seams formed, which crosscut both type 3A crack-seals and type 3B joints. Finally, type 3D faults of  $D_5$  were cemented by calcite cement C5, which consists of microsparite calcite crystals with bright orange luminescence that shows a  $\delta^{18}\text{O}$  value of  $-5.8$  ‰ VPDB and a  $\delta^{13}\text{C}$  value of  $-7.7$  ‰ VPDB.

Finally, in the Sariol outcrop, no evidence of chloritization is observed and deformation occurred in both foot-wall and hangingwall of the Hospital fault, unlike the previous outcrops. Uniquely, two deformation phases have been identified  $D_2$  and  $D_5$ .  $D_2$  is represented by the formation of a dilatant breccia in a type 2 inverse fault affecting the granodiorite. It is cemented by dull to bright orange twinned calcite C2b and C2c crystals (Fig. 5h) with  $\delta^{18}\text{O}$  values about  $-6$  ‰ VPDB and  $\delta^{13}\text{C}$  values about  $-7.2$  ‰ VPDB. During  $D_5$ , type 3D normal faults were generated producing cataclasites in the previous random

breccia and in the Triassic calcitized dolostone of the hangingwall. These cataclasites are cemented by calcite-dolomite cement C6 (Fig. 5i), which has  $\delta^{18}\text{O}$  values about  $-3$  ‰ VPDB and  $\delta^{13}\text{C}$  values about  $-7.6$  ‰ VPDB. Finally, the Hospital fault was cemented by calcite PC1 forming a palisade.

#### Chlorite and white mica petrography

As P–T conditions are estimated from chlorite and mica equilibrium, a brief petrographic description of these minerals is required.

Two groups of K-white mica have been texturally differentiated. The first group is formed by the coarse idiomorphic K-white mica, associated with microcline, which is observed in the slightly brecciated granodiorite of the Vallès fault. It is between 0.2 and 1.1 mm long, and it is formed by a residual core with marked cleavage (M1) rimmed by another white mica with poor cleavage (M2) (Fig. 6a). The second group is constituted by later small grains of K-white mica between 15 and 90  $\mu\text{m}$  in size that crystallize along type 1 faults crosscutting or overgrowing detrital flakes of the previous mica (Fig. 6b). They also crystallize together with chlorite in type 1 faults (Fig. 6c, d). These small mica grains are named M3 and M4 according to chemical criteria (see “K-white mica” section).

Also, two types of chlorite were identified texturally. The first one is the result of biotite alteration, and it is only identified in the fault core formed during  $D_1$  of the Hospital outcrop. These chlorites are recognized by the alternation with sheets of biotite, their prismatic morphology and/or the marked cleavage of the previous biotite (Fig. 6e). They have a strong pleochroism from yellow to bright or dark green.

The second type is constituted by newly formed chlorites that precipitate in type 1 and type 3A faults or as patches in the cataclasite matrix of both Vallès and Hospital faults (Fig. 6c, d, f). They are larger when precipitate in fractures (200  $\mu\text{m}$ –1 mm) than in the cataclastic matrix (7–150  $\mu\text{m}$ ) (Fig. 6d, f). This chlorite usually shows an irregular and ameboid morphology and has slight or no pleochroism.

#### Thermobarometric results

##### Chemical variations and thermobarometry

##### K-white mica

K-white mica analyses have been plotted into the ternary diagram celadonite ( $\text{K}(\square)(\text{Mg},\text{Fe})\text{AlSi}_4\text{O}_{10}(\text{OH})_2$ ), muscovite ( $\text{K}(\square)\text{Al}_3\text{Si}_4\text{O}_{10}(\text{OH})_2$ ) and pyrophyllite ( $(\square)\text{Al}_2\text{Si}_4\text{O}_{10}(\text{OH})_2$ )

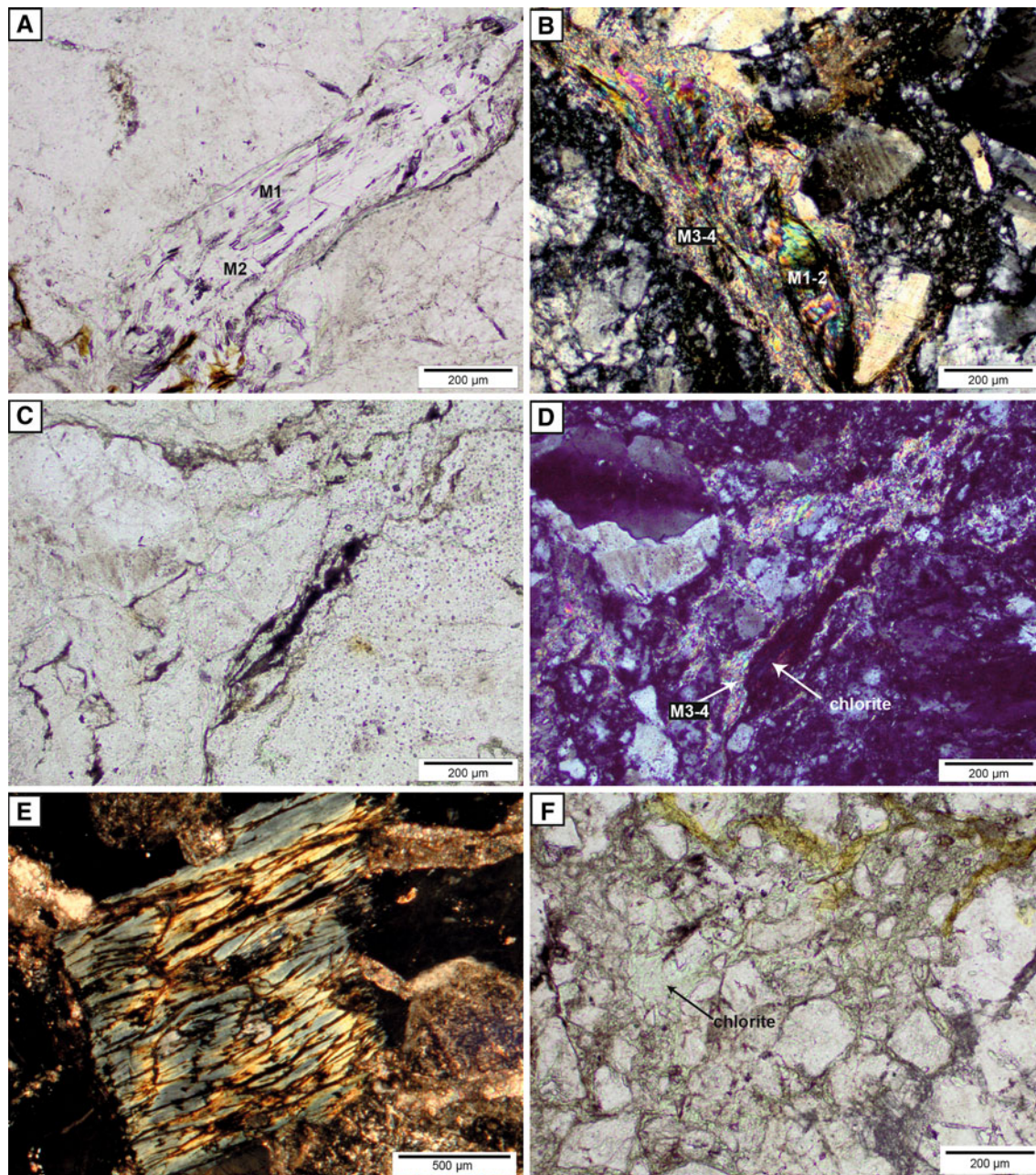


**Fig. 6** Microphotographs of chlorite and mica from Hospital and Vallès faults. **a** Coarse white mica M1 rimmed by M2. **b** Small white mica flakes overgrowing and crosscutting big detrital flakes of M1 and M2 mica. **c, d** Plane and cross polarized light photographs of

newly formed chlorite and mica association in a type 1 fracture. **e** Chlorite resulting from biotite alteration. **f** Newly formed chlorite between cataclasite clasts. Observe that grain size is smaller than chlorites growing in planes as observed in (c, d)

(Fig. 7). The two groups of K-white mica previously described, coarse idiomorphic mica (M1–M2) and later small grains (M3–M4), show muscovite/pyrophyllite ratios of  $0.92 \pm 0.02$  and  $0.85 \pm 0.03$  %, respectively, being M1–M2 mica muscovite richer than M3–M4 mica. Moreover, independently from this ratio, both groups show the same trend, which is marked by an increase in the celadonite proportion associated with a decrease in muscovite and pyrophyllite end-member proportions from M1 to M2 and M3 to M4,

respectively, defining the four mica subgroups (black arrows in Fig. 7 corresponding to two different growing events). The small flakes that postdate M1–M2 mica are named M3 and M4, where M4 are the celadonite-rich ones. These two trends correspond to two growing events characterized by different mica shapes, P–T conditions and probably bulk rock compositions. Representative K-white mica compositions of each group and the corresponding structural formulas are listed in Table 2.

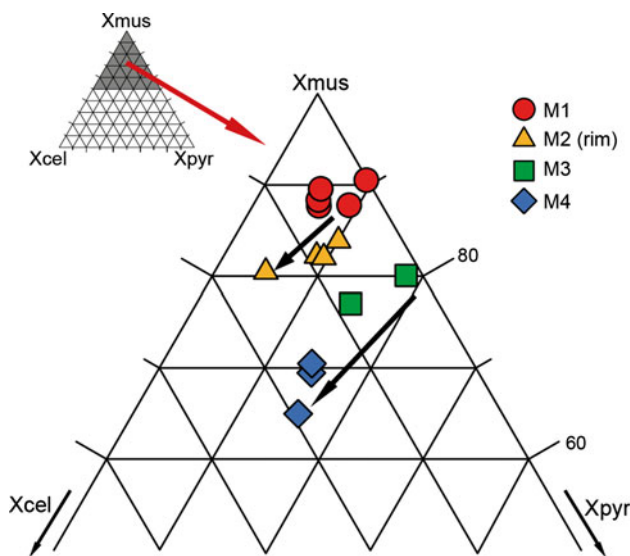


**Fig. 7** Ternary plot muscovite (mus)-celadonite (cel)- pyrophyllite (pyr) of mica in fault rocks of the Vallès fault

**Table 2** Representative K-white mica analysis and atom site distribution for each mica groups

	M1 (n = 5)	M2 (n = 12)	M3 (n = 11)	M4 (n = 4)
SiO <sub>2</sub>	46.85	43.58	48.34	50.69
Al <sub>2</sub> O <sub>3</sub>	35.01	29.98	31.45	29.99
FeO	2.18	2.7	2.76	2.2
MnO	0.03	0.06	0.06	0.01
MgO	0.52	1.21	1.72	2.12
CaO	0.04	0.08	0.07	0.12
Na <sub>2</sub> O	0.86	0.39	0.47	0.2
K <sub>2</sub> O	9.87	9.14	9.39	9.67
<i>Atom site distribution (11 anhydrous-oxygen basis including Fe<sup>3+</sup>)</i>				
Si(T1 + T2)	3.11	3.17	3.22	3.35
Al(T2)	0.89	0.83	0.78	0.65
V(M1)	0.98	0.98	1.00	0.98
Mg(M1)	0.01	0.01	0.00	0.01
Fe <sup>2+</sup> (M1)	0.02	0.01	0.00	0.01
Al(M2 + M3)	1.85	1.73	1.68	1.69
Mg(M2 + M3)	0.04	0.12	0.17	0.2
Fe(M2 + M3)	0.1	0.15	0.07	0.12
K(A)	0.84	0.85	0.8	0.82
Na(A)	0.11	0.05	0.06	0.03
V(A)	0.05	0.09	0.14	0.15

*n* number of analysis done in each generation

A P–T line corresponding to the equilibrium between K-white mica, quartz and water was calculated for each mica composition using the method proposed by Dubacq et al. (2010). There is not significant change in pressure from the granodiorite emplacement (1.5 kbar) to the

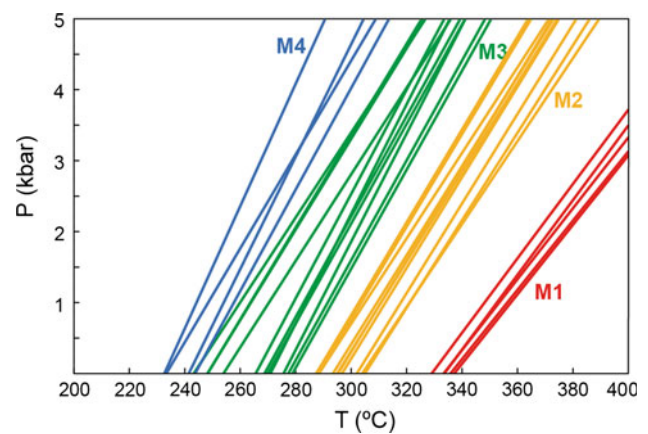


**Fig. 8** P–T diagram showing the results of mica-quartz-water thermometer for the four groups of mica

Neogene extension (0.7 kbar). At a fixed pressure, temperature decreases from M1 to M4 mica (Fig. 8).

### Chlorite

The chlorite compositions were plotted into a (Mg, Fe)-amesite, clinocllore + daphnite and (Mg, Fe)-sudoite ternary diagram, using the structural formulas calculated with the Fe<sup>3+</sup> content predicted by the convergence of R1–R4 (see below). The chlorite compositions evolve along a trend corresponding to a decrease in amesite, clinocllore and daphnite and an increase in sudoite end-member proportion. Sudoite proportion increases from 0.2 to 0.6 in the Vallès fault and 0.2–0.45 in the Hospital fault (Fig. 9). Representative chlorite compositions and corresponding structural formulas are listed in Table 3.

The chlorite-quartz-water equilibria (R1–R4) are located at temperatures between 125 and 310 °C in the Vallès fault and between 240 and 310 °C in the Hospital fault at 1 kbar (absolute error about ±50 °C) (Fig. 10a, b). The temperature histograms allow to differentiate different groups of chlorites, which are dependent on chemical criteria and do not correlate with the types of chlorites differentiated texturally. Four groups of chlorites were identified within the Vallès fault: CHL1 from 260 to 310 °C (XFe<sup>3+</sup> = 0.24), CHL2 from 240 to 260 °C (XFe<sup>3+</sup> = 0.28), CHL3 from 190 to 240 °C (XFe<sup>3+</sup> = 0.33), and, CHL4 from 125 to 190 °C (XFe<sup>3+</sup> = 0.41). The former two groups, CHL1 and CHL2, were also identified in the Hospital fault. The chlorite crystallization temperatures were estimated at 1 kbar due to regional constraints. Changing the value of pressure within +1 kbar does not change significantly the temperature estimates, because equilibria R1–R4 are mostly dependent on T over this range of P–T conditions. The comparison of the temperatures estimated with the chlorite-quartz-water method and with the independent

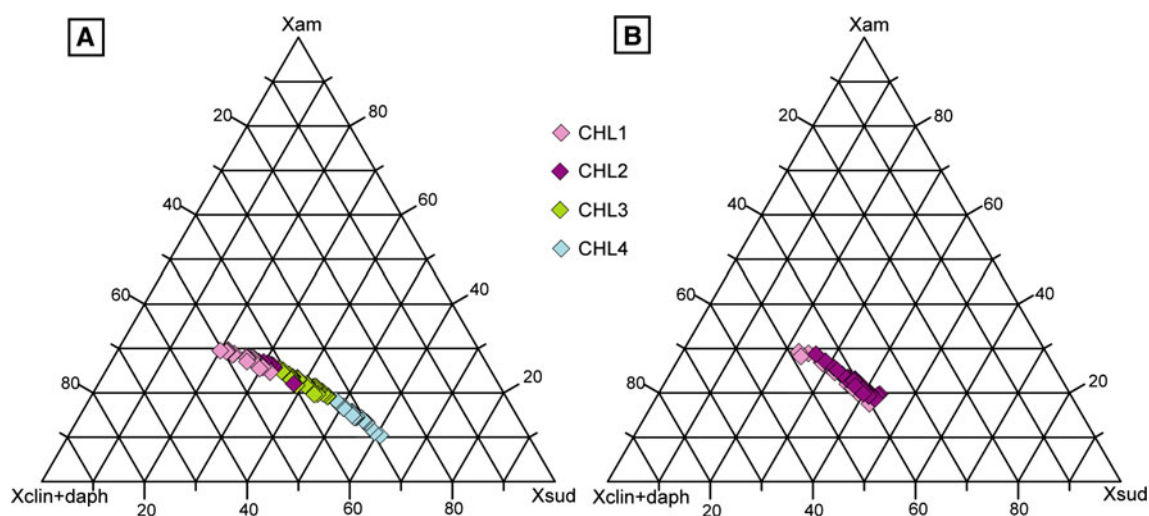


**Fig. 9** Ternary plot amesite (am)-clinochlore + daphnite (clin + daph)- sudoite (sud) of chlorite in fault rocks. **a** Vallès fault. **b** Hospital fault. Colors indicates temperature according to Fig. 9

**Table 3** Representative chlorite composition, atom site distribution and temperature estimate for the different chlorite generations of both faults

Vallès fault				Hospital fault				
Neoformed				From biotite				
Chlorite generation	CHL1 (n = 19)	CHL2 (n = 17)	CHL3 (n = 42)	CHL4 (n = 19)	CHL1 (n = 15)	CHL2 (n = 7)	CHL1 (n = 17)	CHL2 (n = 13)
SiO <sub>2</sub>	26.3	26.62	27.03	28.47	26.39	27.99	26.81	27.26
Al <sub>2</sub> O <sub>3</sub>	21.8	21.42	21.62	21.68	17.6	19.09	17.73	18.44
FeO	26.92	25.84	25.36	25.8	27.53	24.26	24.83	27.41
MnO	0.46	0.52	0.59	0.55	0.78	0.42	0.73	0.64
MgO	13.18	13.55	13.31	11.11	13.44	16.76	15.41	13.56
CaO	0.15	0.1	0.1	0.55	0.06	0.00	0.04	0.06
Na <sub>2</sub> O	0.00	0.02	0.00	0.06	0.03	0.05	0.00	0.00
K <sub>2</sub> O	0.04	0.08	0.02	0.18	0.12	0.00	0.00	0.05
<i>Atom site distribution (14 anhydrous-oxygen basis including Fe<sup>3+</sup>)</i>								
Si(T1 + T2)	2.71	2.73	2.76	2.86	2.79	2.79	2.8	2.81
Al(T2)	1.29	1.26	1.24	1.12	1.21	1.21	1.2	1.19
Al(M1)	0.29	0.26	0.24	0.12	0.21	0.2	0.2	0.19
Mg(M1)	0.25	0.24	0.22	0.17	0.25	0.28	0.28	0.23
Fe <sup>2+</sup> (M1)	0.23	0.19	0.17	0.13	0.17	0.12	0.14	0.15
V(M1)	0.23	0.3	0.37	0.58	0.37	0.4	0.39	0.43
Mg(M2 + M3)	1.78	1.84	1.81	1.5	1.87	2.22	2.12	1.85
Fe <sup>2+</sup> (M2 + M3)	1.69	1.47	1.39	1.17	1.27	0.94	1.03	1.22
Al(M2 + M3)	0.47	0.62	0.74	1.19	0.77	0.8	0.78	0.86
Al(M4)	0.61	0.44	0.39	0.13	0.00	0.03	0.00	0.01
Fe <sup>3+</sup> (M4)	0.39	0.56	0.61	0.87	1.00	0.97	1.00	0.99
XFe <sup>3+</sup>	17	25	28	40	41	48	46	42
Temperature (°C)*	286	256	230	144	286	254	285	256

*n* number of analyses done in each generation

\* Vidal et al. (2005, 2006), see text

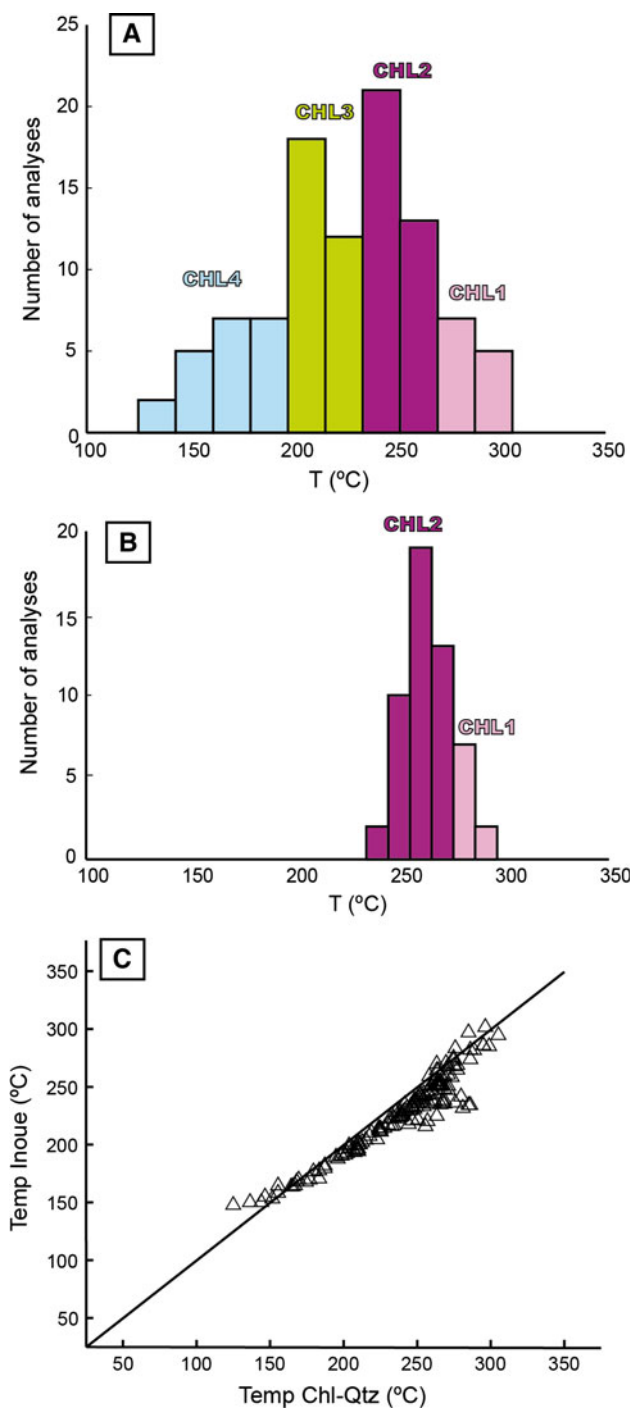


**Fig. 10** Histograms of chlorite temperatures using the chlorite-quartz-water thermometer: **a** Vallès fault and **b** Hospital fault. **c** Comparison of the estimated temperatures with the chlorite-quartz-water thermometer (Vidal et al. 2001, 2005) with those estimated with the semi-empirical thermometer of Inoue et al. (2009). Both approaches show a good correlation and follow the same trend

semi-empirical thermometer of Inoue et al. (2009) demonstrates that the values are similar and follow exactly the same trend (Fig. 10c). This suggests that the estimated  $\text{Fe}^{3+}$  values are realistic because Inoue's

thermometer has been calibrated with measured  $\text{Fe}^{3+}$  contents in chlorite.

The relationships of the chlorite groups with the structural locations are not easy to identify due to the complexity of the recrystallization of chlorite at low temperature (see example in Lanari et al. 2012). However, some 3A faults are mainly filled by low-temperature chlorites (corresponding to the CHL4 group) and most of these chlorites form a rim around high-T chlorites (CHL1–CHL3 groups), indicating their later formation.

The uncertainty on the chlorite temperature steaming from the analytical error was investigated in order to verify that the groups of composition-temperature identified above were not an artifact resulting from the analytical uncertainties of the EPMA measurements. A Monte Carlo method was used: 1,000 compositions of chlorites were randomly simulated from the average group compositions using a normal distribution. The simulated distribution was set in order to reproduce the measured precision at  $\pm 1\text{wt } \%$ . The temperature and  $\text{Fe}^{3+}$ -content of each composition was estimated and the results are plotted in the Fig. 11. The estimated temperatures of the groups of chlorite in the Vallès fault are  $283 \pm 20.4$ ,  $253 \pm 13.0$ ,  $228 \pm 11.7$  and  $142 \pm 13.1$  °C (Fig. 11a). The temperatures of the two groups in the Hospital fault are  $307 \pm 17.7$  and  $245 \pm 7.7$  °C (Fig. 11b). These results show that the identified groups of chlorites correspond to true distinct groups of composition and temperature of formation. The above Monte Carlo analysis does not take into account the errors resulting from the uncertainties of the thermodynamic data, which cannot be assessed. However, it is emphasized that such errors have a systematic effect on the absolute temperature, but not on the relative values of the chlorite groups. This is the reason of using an absolute uncertainty on the temperature estimates of  $\pm 50$  °C.

#### P–T estimates

Chlorite-mica-quartz-water multi-equilibrium approach was applied to chlorite and mica of the Vallès fault. Only equilibrium between chlorite and M3 and M4 mica was obtained, which is coherent with the petrographic observations, as only these mica show structural and spatial relationships with chlorite (“Chlorite and white mica petrography” section). However, chlorites with temperatures below 190 °C have no equilibrium with mica.

The P–T estimates from the chlorite-mica multi-equilibrium show groups of chlorite-mica associations coherent with the previously established chlorite groups (results are plotted with the same colors in Fig. 12a). The first association is defined by the equilibrium between chlorite and M3 mica and ranges from 260 to 310 °C at pressures between 0 and  $3.5 \pm 2.5$  kbar. The second is defined by the

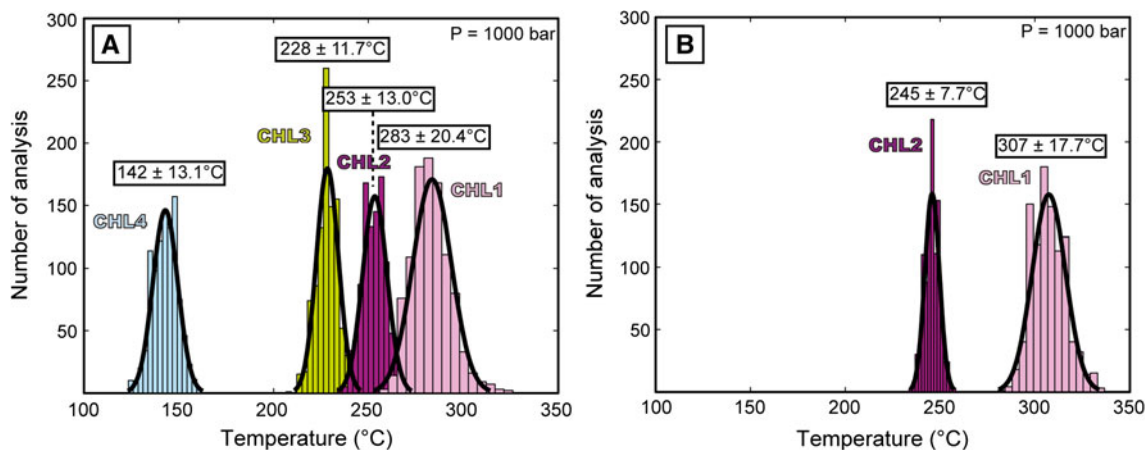


**Fig. 11** Histogram of chlorite temperature for each group of chlorite calculated with the compositions from the Monte Carlo simulation (see text). The colors are the same as in Fig. 9

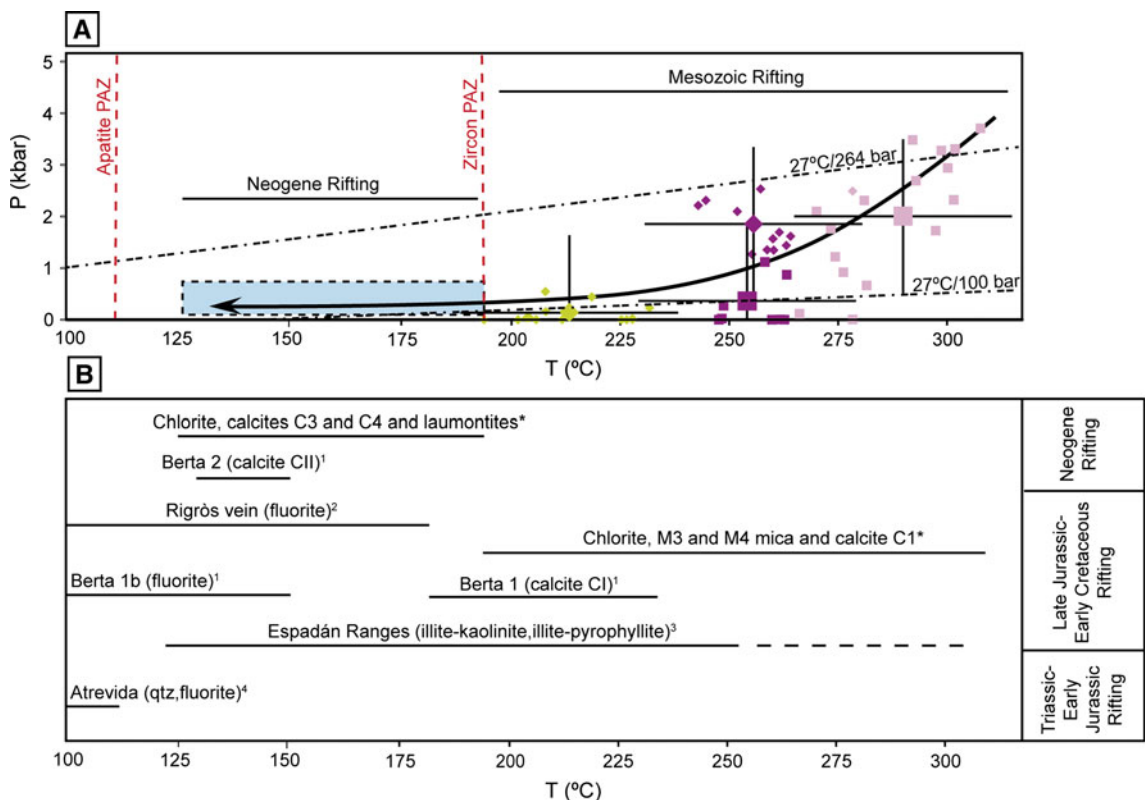


**Fig. 12 a** P–T path of fault rocks in the Vallès fault and interpretation of the age through fission-track constraints. *Squares* represent chlorite in equilibrium with M3 mica and *diamonds* represents chlorite in equilibrium with M4 mica (*error bars* for average values of each chlorite-mica group are  $\pm 20$  °C and  $\pm 1.5$  kbar). The different colors represent the four chlorite groups. The *blue square* indicates the location of chlorites under 190 °C, which are not in equilibrium

with mica. Lithostatic and hydrostatic gradients were calculated considering a Mesozoic geothermal gradient of 27 °C/km according to Juez-Larré (2003). **b** Temperature and age comparison with other mineralizations of the Catalan Coastal Ranges (Berta, Rigròs and Atrevida) and the Iberian Chain (Espadán Ranges). The *asterisk* marks our data. 1 Cardellach et al. (2002); 2 Piqué et al. (2008); 3 Martín-Martín et al. (2006, 2008, 2009); 4 Canals et al. (1992)

equilibrium between chlorite and M3 and M4 mica. This stage ranges from 240 to 260 °C at P between 0 and 1  $\pm$  2.5 kbar with M3 and P between 1 and 3 kbar with M4. Finally, the third group is defined by chlorite in

equilibrium with M4 mica. The P–T conditions of this stage ranges from 190 to 240 °C at pressures between 0 and 0.6  $\pm$  2.5 kbar. P–T uncertainties of 2.5 kbar and 50 °C correspond to the cumulative uncertainties steaming

from analytical errors and uncertainties generally assumed in the context of higher pressure and temperature metamorphic rocks. These uncertainties cannot be calculated rigorously because the individual uncertainties on the standard state properties of the end-members and Margules parameters cannot be estimated. Nevertheless, the difference between the minimum and maximum calculated pressure and temperature values in each group are less than 2 kbar and 30 °C, respectively, except for group CHL1-M3 (4 kbar and 40 °C), as shown in Fig. 12a.

## Discussion

### Origin of K-white mica

M1 mica rimmed by M2 mica conform coarse idiomorphic and muscovite-rich K-white micas, resembling result of crystallization from an igneous origin. However, two-mica granodiorites have never been described in the area (Enrique 1990). The formation of this kind of well-developed crystals has been described as resulting from deuteric alteration during cooling (Demange et al. 1996) by igneous water-rich fluids when the igneous mass was already solidified. This alteration affects preferentially the fractured pluton rims (Shelley 1983). Therefore, M1 K-white mica might be formed in thermal joints produced during the Permian exhumation of the granodiorite at maximum temperatures of 370 °C (estimated temperature at 1.5 kbar, conditions of granodiorite emplacement). Progressive exhumation yielded M1 mica to be re-equilibrated to M2 mica at temperatures above 290 °C according to the exposure of the pluton previous to Triassic, as denoted by the unconformity between the granodiorite and Buntsandstein facies outcropping in the area (Gómez-Gras and Ferrer 1999). Later M3 and M4 phengite crystallize in fractures crosscutting or overgrowing detrital flakes of M1 and M2 mica and have higher pyrophyllite/muscovite ratio than M1 and M2 muscovite. This increase in the pyrophyllite proportion is produced by pyrophyllitic substitution ( $\text{Si} \square \text{K}_{-1} \text{Al}_{+1}$ ). Taking into account their formation in fractures, the crystallization of pyrophyllite-rich mica is probably controlled by the circulation of externally derived fluids and a localized increase in pressure due to tectonic stress in the fault core.

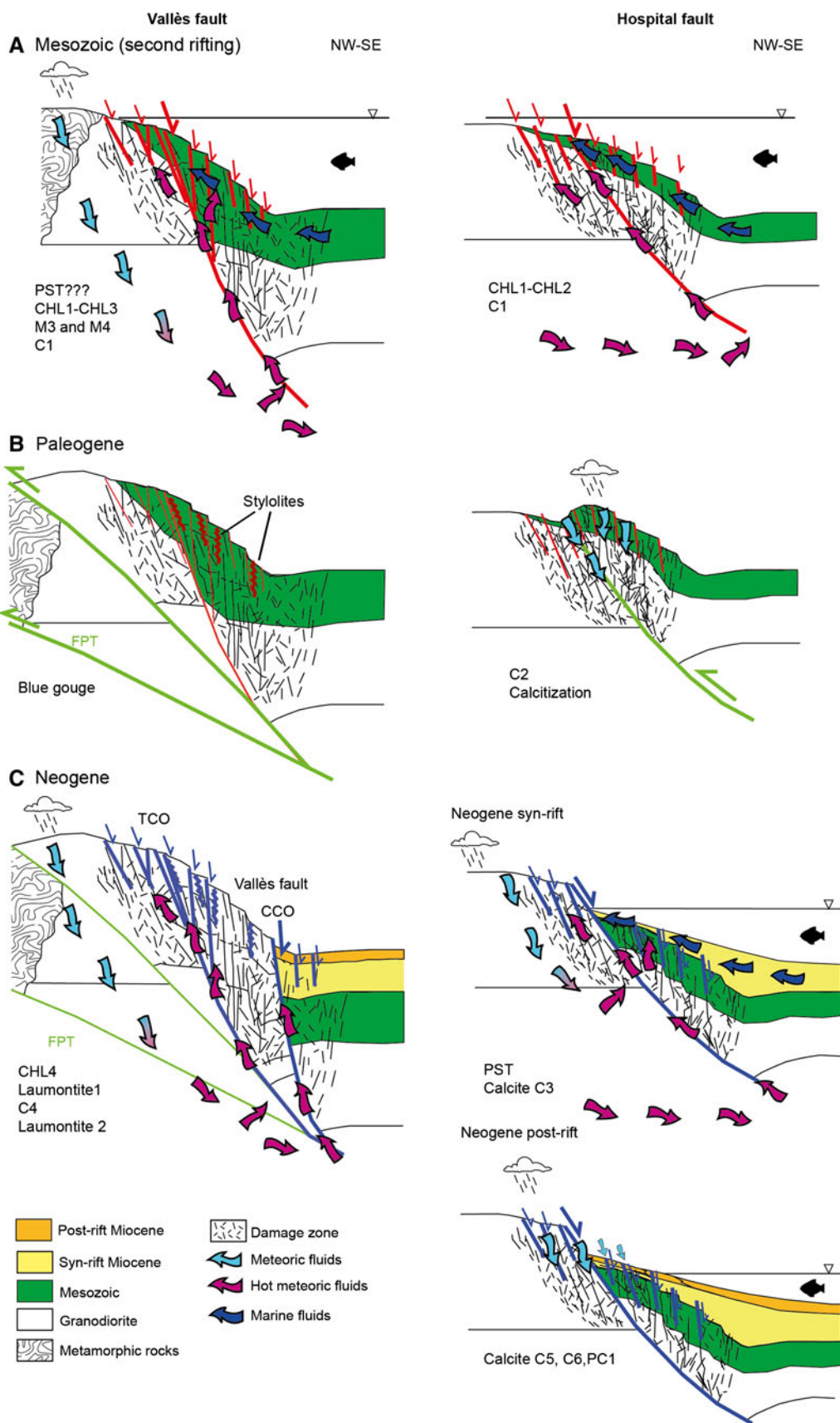
Although the granodiorites in the footwalls of the Vallès and the Hospital faults have the same texture and composition, crystallization of M1 and M2 mica has only been observed in the Vallès fault. This fact probably indicates that the outcrops of the Vallès fault were near the pluton border whereas the outcrops of the Hospital fault were in an inner position or in a less fractured zone. In the same way, the high density of fractures close to the pluton border

would have been the responsible of the thicker fault zone in the Vallès fault (60 m) in front of the narrower Hospital fault zone (1–3 m). As mentioned previously, later M3 and M4 phengite are texturally and spatially related to M1 and M2 muscovite. Therefore, the crystallization of M3 and M4 phengite is conditioned by the presence of previous M1 and M2 coarse muscovite, which change the bulk rock composition of the granodiorite that is necessary for the neoformation of the late K-white mica groups.

The coincidence between the localization of Hercynian fractures with M1 and M2 muscovite and the Vallès fault suggests that this fractured zone of the granodiorite was used for the later development of the Vallès fault. In the Enric outcrop (Hospital fault, see Fig. 1), Cenozoic and Mesozoic deformation overprints previous bands of dynamically recrystallized quartz-feldspathic rocks, indicating therefore the reactivation of Hercynian structures, which has not been described previously in the Catalan Coastal Ranges.

### Interpretation of P–T estimates linked to main tectonic events

The petrological study together with P–T estimates show that fault zones followed a continuous retrograde path through time (Fig. 12a). The constraints obtained from fission-track studies allow us to associate the different chlorite groups with the several tectonic events involved in the formation of the Catalan Coastal Ranges. Fission-track and (U–Th)/He studies with apatites and zircons in this sector of the Catalan Coastal Ranges show that the 190 °C isotherm (closure temperature for zircon PAZ) was crossed during Mesozoic extension (Juez-Larré 2003). This observation locates the neoformation of M3 and M4 phengite and related chlorite, and by extension the first deformation phase ( $D_1$ ), to this extensional tectonic event (Fig. 12). However, two rift stages followed by their relative post-rift stages occurred during the Mesozoic. In order to delimit the formation of M3–M4 phengite and related chlorites inside one of these rift stages, our data were compared with other works on hydrothermal veins in the Catalan Coastal Ranges and the Iberian Chain (Fig. 12b). Temperatures between 190 and 230 °C in calcites (calcites CI, in Cardellach et al. 2002) have been attributed to the second Mesozoic rifting in the Berta mine (Montnegre Horst, Fig. 1). These calcites have the same isotopic characteristics as the calcites C1 defined in this work. Temperatures between 120 and 300 °C have been also assigned to the second Mesozoic rift stage from illite-kaolinite and illite-pyrophyllite associations within the Permo-Triassic rocks of the Espadán Ranges (Iberian Chain) (Martín-Martín et al. 2008). Both comparisons would point to the formation of chlorite ( $T > 190$  °C), K-white mica M3 and M4



◀ **Fig. 13** Evolution of the Vallès and Hospital faults from Mesozoic to Neogene. **a** Mesozoic extensional event. Topographically driven meteoric fluids, percolating in emerged areas, are warmed at depth and upflow through faults. Due to the submarine conditions of the major part of the basin, these fluids are mixed with marine waters at surface. **b** Paleogene compressional event. In the Vallès fault a thrust system uplifts the previous normal fault. Deformation is localized in the thrust faults generating a blue gouge. In the Hospital fault, the previous Mesozoic fault is inverted and percolation of low-T meteoric waters occurs. **c** Neogene extensional event. During this event, the Neogene normal Vallès fault is formed (CCO) and the reactivation of some of the Mesozoic structures occurs (TCO). Hydrothermal fluids are topographically driven meteoric fluids warmed at depth. In the hospital fault, syn-rift and post-rift stages differ. During the syn-rift, meteoric hot fluids are mixed with marine waters, as occurred during the Mesozoic. On the opposite, the post-rift is dominated by low-T meteoric fluids. TCO Torrent del Corró outcrop, CCO Camí d'en Cisa outcrop, FPT Frontal Paleogene thrust

and calcite C1 to this second Mesozoic rift stage (Late Jurassic–Early Cretaceous). The  $\delta^{18}\text{O}$  composition of the fluid responsible of the precipitation of these cements was calculated through the modified equation of Craig and Gordon (1965), obtaining values between +7 and +10 ‰ SMOW. Taking into account that the  $\delta^{18}\text{O}$  composition of granodiorites is about +10 ‰ SMOW, the origin of these fluids has been interpreted as meteoric waters that have been warmed at depth, previously to their upflow through faults, and that have been completely buffered by the granodioritic host rock. Moreover due to the submarine conditions in most of the basin during this extensional event, these fluids were mixed with marine waters during their upflow (Cantarero et al. 2013) (Fig. 13a). This mixing could explain the cathodoluminescence oscillations (bright to dull orange) of calcites C1.

The timing of low-temperature chlorite (125–190 °C) growth is more difficult to assess. The temperature conditions of LT chlorite crystallization were achieved during both the second Mesozoic rifting stage and the Neogene extension, as denoted by fission-track and fluid inclusion studies. Fission-track studies demonstrated that the 110 °C isotherm (closure temperature for apatite PAZ) was crossed at the onset of the Neogene extension. On the other hand, studies of fluid inclusions in veins of the Catalan Coastal Ranges have obtained temperatures between 110 and 190 °C in Mesozoic fluorites (i.e., Rigròs vein) and in Neogene calcites (calcites CII, in Cardellach et al. 2002) (Fig. 12). Fluorites are not present in the studied outcrops whereas calcite is a common neoformed mineral. Moreover, these Neogene calcites (CII) show similar geochemical characteristics than the calcites C3 and C4 defined in this paper. Therefore, LT chlorite crystallization (+calcites C3 and C4 and laumontite) and type 3A and 3B fractures, where most of these cements precipitated, might take place during the Neogene extensional event. From the  $\delta^{18}\text{O}$  isotopic composition of calcites C3 and C4 (–20 and

–24 ‰ VPDB, respectively) and a medium value of temperature obtained from chlorite (150 °C), the origin of the parental fluid of these cements can be inferred applying the modified equation of Craig and Gordon (1965). The results are fluids with  $\delta^{18}\text{O}$  values about 0 ‰ SMOW for C3 and –4.1 ‰ SMOW for C4. These fluids have been interpreted as meteoric fluids that have been warmed at depth and later have upflowed through the main faults. During flow, these fluids have suffered a strong interaction with host rocks, especially the granodiorite, causing the buffering of their isotopic signal. Moreover, in the Hospital fault, due to its position close to the Miocene shoreline, these fluids could have been mixed with marine water yielding to their more positive values (Fig. 13).

Nowadays, hot springs along the Vallès fault have superficial temperatures up to 70 °C and calculations of the reservoir temperature reach 110–120 °C (Trilla 1974; Albert 1975). From reservoir temperature and the  $\delta^{18}\text{O}$  value of these thermal waters, –7 ‰ SMOW according to Trilla (1974), the  $\delta^{18}\text{O}$  content of the calcites that could precipitate nowadays would be about –23 ‰ VPDB, value of calcites C4. In turn, calcite C4 is related to the presence of laumontite. The stability of laumontite is constrained at very low carbon dioxide contents in the solution (mole fraction of  $\text{CO}_2$  below 0.1) and neutral to slightly alkaline waters in conditions of low pressure and low temperature (Liou et al. 1985). The present-day thermal waters of Caldes de Montbui have pH values between 7.9 and 8.35 and values of dissolved  $\text{CO}_2$  of 0.88 mg/l, yielding in the laumontite stability field. In fact, the precipitation of calcite C4 or laumontite is caused by very low fluctuations in the  $\text{CO}_2$  content of waters, as laumontite is very sensitive to these variations (Ivanov and Gurevich 1975). Thus, hydrothermalism in the Vallès fault has remained active from the onset of the Neogene extension up to nowadays characterized by the precipitation of calcite C4, laumontite and LT chlorite. In contrast, hydrothermalism in the Hospital fault only took place during the Neogene syn-rift stage, as shown by precipitation of calcite C3. The later deformation stages of the Hospital fault associated with the post-rift, from  $D_5$  to  $D_7$ , were characterized by low-temperature fluids responsible of precipitation of calcites C5, C6 and PC1 (Cantarero et al. 2013).

According to previous works, maximum burial of the studied outcrops during the three tectonic events reached 3.6 km before the Paleogene compression and 2.2 km before the Miocene extension (e.g., Juez-Larré 2003, ter Voorde et al. 2007). Thus, the estimated pressures above 1.5 kbar are not directly related to and compatible with burial conditions. Figure 12a shows that most P–T pairs fall between the hydrostatic and lithostatic gradients drawn for the Mesozoic. This might be indicative of episodic variations of fluid pressure (Pf) expected in faults and hydrothermal systems

due to cementation and reopening of veins (Sibson et al. 1988; Fournier 1991; Sibson 2000), or of abnormal pressures following abrupt changes of temperature in isolated systems with time (Barker 1972). However, several P–T points in Fig. 12 plot at pressures below the hydrostatic gradient or above the lithostatic gradient. It is therefore more likely that the scatter in the calculated pressure reflects uncertainties and cumulative errors associated with the method of calculation. The distribution of pressure shown in Fig. 12 suggests a minimum uncertainty of  $\pm 1.5$  kbar and 20 °C, which is lower than the  $\pm 2.5$  kbar, 50 °C cumulative uncertainties commonly assumed for metamorphic rocks. Average P–T conditions are reported for the different groups in Fig. 12 with large symbols (212 °C–0.10 kbar (CHL3-M4), 257 °C–1.87 kbar (CHL2-M4), 256 °C–0.29 kbar (CHL2-M3) and 287 °C–2.04 kbar (CHL1-M3)) with  $\pm 1.5$  kbar and 20 °C error bars. These average P–T conditions suggest that pressure is possibly lower in groups CHL3-M4 and CHL2-M3 than in groups CHL2-M4 and CHL1-M3 but the differences are within the uncertainty of calculation. Pressure is possibly higher in the highest temperature group (CHL1-M3), which shows the highest spread in P–T conditions and a correlated decrease in P and T (in contrast to the lower temperature groups). This trend might indicate a change of P–T conditions during the beginning of the Late Jurassic–Early Cretaceous rifting stage. In the limit of the uncertainties discussed above, and although the evolution of pressure is weakly constrained, our results point to a general decrease in pressure from 4 kbar at 287 °C to about 100 bar at 210 °C (solid arrow in Fig. 12). This proposed P–T evolution is consistent with the tectonic evolution of the Vallès fault. On one hand, deformation is located in the footwall of the fault. During extensional tectonics the footwall is exhumed due to isostatic rebound and consequent erosion of the shoulder. On the other hand, the traces of the Paleogene thrust and the normal fault are not coincident in surface but the former is displaced to the north (Anadón 1986). Therefore, the previous normal fault was located in the hangingwall of the thrust and was uplifted during thrusting. This divergence between the compressional and extensional structures also explains the lack of microstructures and cements linked to compression overprinting the Mesozoic fractures of the Vallès fault (Fig. 13). Instead, it is produced the blue gouge in type 2 thrust faults during the second deformation phase. On the opposite, in the Hospital fault, the Mesozoic fault is inverted during the Paleogene, as registered by the low-temperature calcite cements C2 in type 2 thrust faults (Fig. 13).

#### Migration paths of fluids along main faults

Along both the Vallès and Hospital faults, different neoformed mineral associations are evidenced (Fig. 4). This

could be due to fault zone architecture changes, inherited structures, independent tectonic activity of fault segments and/or localized migration paths of certain fluids.

In the Hospital fault, these differences in neoformed minerals were mainly interpreted as a result of the different origin of the fault segments during the Mesozoic and their later independent tectonic activity during the Mesozoic, Paleogene and Neogene (Cantarero et al. 2013).

In the Vallès fault, these differences are attributed to the different structural position of the outcrops within the footwall. The Camí d'En Cisa outcrop is located in the tectonic contact with the Miocene rocks, and only the formation of laumontite L2 related to the Neogene extension is registered. On the other hand, the Torrent del Corró outcrop, located 50 m from the contact, shows all the deformation stages, mainly chlorite-mica, chlorite and calcite veins. As mentioned above, mica-chlorite veins and calcite C1 have been related to the Mesozoic extension, whereas low-T chlorite, laumontite and calcite C4 have been related to the Neogene extension. This means that the TCO outcrop represents the location of a Mesozoic fault zone reactivated during the Neogene deformation. These observations point to an offset between the Mesozoic and the Neogene faults (Fig. 13). Furthermore, most of the low-T chlorites (125–190 °C group) form a rim around high-T chlorites ( $T > 200$  °C), indicating the reactivation of the Mesozoic structures with phyllosilicates during the Neogene. This reactivation was possible due to the low friction coefficient of chlorite and K-white mica and their arrangement in localized fracture planes under hydrated conditions (Lacroix 2011; Behnken and Faulkner 2012; Buatier et al. 2012a, b). Probably, the absence of Neogene chlorite within the Hospital fault is due to the lack of a strong preferred orientation of chlorite crystals together with the lack of connection between them within the foliation.

#### Implications on the geothermal gradient

The estimated high temperature formation of chlorite and K-white mica (125–310 °C) together with the formation temperature of laumontite (100–230 °C, Kristmannsdóttir and Tómasson 1978), and linked to depth constraints, imply geothermal gradients higher than the regional gradients during the two extensional tectonics events. According to our data, geothermal gradients during the Mesozoic ranged between 55 and 83 °C/km and from 56 to 86 °C/km during the Neogene. These values are much larger than the regional gradients estimated on the basis of the thermal boundary conditions and thickness of the lithosphere and the thermal conductivity of materials by Juez-Larré (2003) (27–35 °C/km in the Mesozoic and  $24 \pm 3$  °C/km in the Neogene). The main hydrothermal

processes during Neogene were assumed to take place at the onset of extension as it was marked by fission-track data, and therefore, the depth previous to the extensional process was taken for calculations. However, evidence of hot fluids associated with faults has been also described during the Neogene post-rift (Calvet et al. 1996, 2001) in the Penedès basin fill and nowadays in the Caldes de Montbui area (López de Azcona 1983). Important exhumation was already achieved at the post-rift stage, which linked with the hydrothermalism, would even cause higher geothermal gradients.

The difference between regional gradients and our data suggests that during both extensional tectonic events, faults acted as conduits for ascending hot fluids, which produced anomalous high geothermal gradients along fractures. This fact is also supported by the resetting of fission-tracks mostly near main fault zones limiting the grabens (Juez-Larré 2003).

## Conclusions

The Vallès and Hospital faults are two of the main faults that constitute the central sector of the Catalan Coastal Ranges. In these faults, deformation is localized in the granodiorite that constitutes the footwall where different fault rocks, from breccias to ultracataclasites, are formed.

Six deformation phases have been related to the three main tectonic events described in the area through structural and petrographic studies, thermodynamic modeling from chlorite and phengite, and fission-track constraints. In the Vallès fault, previously to the first tectonic event, crystallization of muscovite-rich M1 and M2 K-white mica took place as a result of deuteritic alteration during the exhumation of the pluton, which ended in the Permian, at temperatures between 290 and 370 °C.

The first tectonic event is attributed to the Mesozoic extension, and it is represented by the first deformation phase ( $D_1$ ). In the Vallès fault,  $D_1$  is characterized by the crystallization of M3 and M4 phengite together with chlorite at temperatures between 190 and 310 °C and calcite C1. In the Hospital fault, only chlorite formed at temperatures between 240 and 310 °C together with calcite C1.

The second tectonic event is related to the Paleogene compression, and it is defined by the second deformation phase ( $D_2$ ). Low-temperature calcite cements belonging to the Paleogene compression have been identified in the Hospital fault, whereas in the Vallès fault, deformation is concentrated along the shortcut, avoiding the reactivation of the Mesozoic structures.

Finally, the third tectonic event is associated with the Neogene extension. Four deformation phases have been

recognized ( $D_3$ – $D_6$ ) from which  $D_3$  is related to the syn-rift stage. In the Vallès fault, type 3A normal faults were cemented by chlorite formed at temperatures below 190 °C, associated with calcite C4 and laumontite. Later, these faults were offset by type 3E strike-slip faults. In the Hospital fault, type 3A and 3B fractures were cemented by calcite C3. During the post-rift, calcites C5, C6 and PC1 precipitated.

Both faults have registered two hydrothermal events, one during the Mesozoic and one during the Neogene. However, hydrothermalism has remained active up to recent times only in the Vallès fault. Hydrothermalism in the Hospital fault was restricted to the syn-rift stage, and the post-rift stage was dominated by low-temperature fluids.

The different associations of newly formed minerals along the two main faults is conditioned by (1) *Tectonic processes*: The various origin and later tectonic activity of the segments that form the Hospital fault, and the offset between the Mesozoic and the Neogene faults that constitute the Vallès fault both control the temporal and spatial distribution of fluids and cements. (2) *The rheologic properties of minerals*: The presence of preferentially oriented chlorites concentrated along planes generates a microfabric that weakens the fault. The drop of friction coefficient favors stable sliding and therefore the formation of successive generations of chlorite. (3) *Previous mineralogic compositions*: The existence of previous mineral phases only in certain areas can cause the necessary change in the bulk rock composition to generate a new neofomed mineral (i.e., only where M1–M2 muscovite exist, M3–M4 phengite are formed). Also, small oscillations on the chemical conditions of the fluid can control the precipitating phase (i.e., the calcite–laumontite relationship).

The structural and temporal relationships between M3–M4 phengite and M1–M2 muscovite indicates that Hercynian fractures were reactivated and overprinted by the Mesozoic and Cenozoic development of the Vallès fault. During Mesozoic and Neogene tectonic events, faults acted as conduits for hot fluids producing localized anomalous high geothermal gradients (50 °C/km minimum) along the faults.

The estimated pressure conditions show possible signs of fluid pressure variations and a decrease in pressure consistent with exhumation produced during Alpine compression and Mesozoic and Neogene extensions. During the Neogene extension, exhumation of the granodiorite followed a nearly isobaric cooling path.

**Acknowledgments** We thank Anne-Marie Boullier for discussion and useful comments during thin section description. We are grateful with Jordi Illa for sample preparations and with the Thin Section Service of the Universitat de Barcelona. The stable isotopy, the electron microprobe, and the SEM analyses were carried out at

“Serveis Científico-Tècnics” of the Universitat de Barcelona. The authors also want to thank Delphine Charpentier and an anonymous referee for their constructive reviews, which helped to improve the quality of the manuscript. This research was performed within the framework of DGICYT Spanish Project CGL2010-18260, *Grup Consolidat de Recerca* “Geologia Sedimentària” (2009SGR-1451) and the grants 2010BE1 00708 and 2010FI\_B2 00179 supported by the Comissionat per a Universitats i Recerca del Departament d’Innovació, Universitats i Empresa de la Generalitat de Catalunya i el Fons Social Europeu.

## References

- Agard P, Vidal O, Goffé B (2001) Interlayer and Si content of phengite in HP–LT carpholite-bearing metapelites. *J Metamorph Geol* 19(5):479–496
- Albert JF (1975) El equilibrio albita-anortita como termómetro hidrogeotérmico en zonas graníticas. *Acta Geol Hisp X* 5:170–174
- Albert JF, Corominas J, París C (1979) El estudio hidrogeológico de los manantiales y su aplicación geológica: caso de las aguas termales, carbónicas y sulfídricas de Cataluña. *Acta Geol Hisp Homenatge a Lluís Solé i Sabarís* 14:391–394
- Anadón P (1986) Las facies lacustres del Oligoceno de Campins (Vallès Oriental, Provincia de Barcelona). *Cuad Geol Ibérica* 10:271–294
- Anadón P, Colombo F, Esteban M, Marzo M, Robles MS, Santanach P, Solé-Sugrañes LL (1979) Evolución tectonoestratigráfica de los Catalánides. *Acta Geol Hisp* 14:242–270
- Anadón P, Cabrera L, Guimerà J, Santanach P (1985) Paleogene strike-slip deformation and sedimentation along the southeastern margin of the Ebro Basin. In: Biddle KT, Christie-Blick N (eds) Strike-slip deformation, basin formation sedimentation. *Spec Publ Soc Econ Paleontol Mineral* 37:303–318
- Árkai P, Faryad SW, Vidal O, Balogh K (2003) Very low-grade metamorphism of sedimentary rocks of the Meliata unit, Western Carpathians, Slovakia: implications of phyllosilicate characteristics. *Int J Earth Sci* 92:68–85
- Ashauer H, Teichmüller R (1935) Die variszische und alpidische Gebirgsbildung Kataloniens. *Abhandlungen Gesellschaft Wissenschaften Göttingen. Math Phys Kl*: 3F, 16
- Baqués V, Travé A, Cantarero I (2013) Development of successive karstic systems within the Baix Penedès Fault zone (onshore of the Valencia Trough, NW Mediterranean). *Geofluids*. doi:10.1111/gf.12044
- Barker C (1972) Aquathermal pressuring- role of temperature in development of abnormal-pressure zones. *AAPG Bull* 56(10):2068–2071
- Bartrina MT, Cabrera L, Jurado MJ, Guimerà J, Roca E (1992) Evolution of the central Catalan margin of the Valencia trough (western Mediterranean). *Tectonophysics* 203:219–247
- Behnsen J, Faulkner DR (2012) The effect of mineralogy and effective normal stress on frictional strength of sheet silicates. *J Struct Geol* 42:49–61
- Bitzer K, Travé A, Carmona JM (2001) Fluid flow processes at basin scale. *Acta Geol Hisp* 36(1–2):1–20
- Buatier M, Chauvet A, Kanitpanyacharoen W, Wenk HR, Ritz JF, Jolivet M (2012a) Origin and behavior of clay minerals in the Bogd fault gouge, Mongolia. *J Struct Geol* 34:77–90
- Buatier M, Lacroix B, Labaume P, Moutarlier V, Charpentier D, Sizun JP, Travé A (2012b) Microtextural investigation (SEM and TEM study) of phyllosilicates in a major thrust fault zone (Monte Perdido, southern Pyrenees): impact on fault reactivation. *Swiss J Geosci* 105:313–324. doi:10.1007/s00015-012-0098-0
- Calvet F, Travé A, Roca E, Soler A, Labaume P (1996) Fracturación y migración de fluidos durante la evolución tectónica neógena en el Sector Central de las Cadenas Costero Catalanas. *Geogaceta* 20(7):1715–1718
- Calvet F, Travé A, Bitzer K, Roca E, Tritilla J, Baker J (2001) Dolomitization of detrital deposits related to Neogene extensional faults, Catalan Coastal Ranges (Spain). *Geotemas* 3(1):109–111
- Canals À, Cardellach E (1997) Ore lead and sulphur isotope pattern from the low-temperature veins of the Catalonian Coastal Ranges (NE Spain). *Miner Deposita* 32:243–249
- Canals À, Cardellach E, Rye DM, Ayora C (1992) Origin of the Atrevida vein (Catalan Coastal Ranges, Spain): mineralogic, fluid inclusion and stable isotopy study. *Econ Geol* 87:142–153
- Cantarero I, Travé A, Alías G, Baqués V (2013) From hydrothermal to meteoric fluid regimes in a segmented fault affecting crystalline and carbonate rocks: case study of the Barcelona Plain (NE Spain). *Geofluids*. doi:10.1111/gf.12021
- Cardellach E, Canals À, Grandia F (2002) Recurrent hydrothermal activity induced by successive extensional episodes: the case of the Berta F-(Pb-Zn) vein system (NE Spain). *Ore Geol Rev* 22:133–141
- Carmona JM, Bitzer K, López E, Bouazza M (2000) Isotopic composition and origin of geothermal waters at Caldetes (Maresme-Barcelona). *J Geochem Explor* 69–70:441–447
- Cathelineau M, Nieva D (1985) A chlorite solid solution geothermometer the Los Azufres (Mexico) geothermal system. *Contrib Mineral Petrol* 91(3):235–244
- Collettini C, Niemeijer A, Viti C, Marone C (2009) Fault zone fabric and fault weakness. *Nature* 462:907–911
- Craig H, Gordon I (1965) Deuterium and oxygen-18 variations in the ocean and marine atmosphere. In: Tongiorgi E (ed) *Stable Isotopes in Oceanographic Studies and Paleotemperatures*. Consiglio Nazionale delle Ricerche, Laboratorio di Geologia Nucleare, Pisa, pp 9–130
- Demange M, Alvarez JO, López L, Zarco JJ (1996) The Achala Batholith (Cordoba, Argentina): a composite intrusion made of five independent magmatic suites. Magmatic evolution and deuteric alteration. *J S Am Earth Sci* 9(1–2):11–25
- Dubacq B, Vidal O, de Andrade V (2010) Dehydration of dioctahedral aluminous phyllosilicates: thermodynamic modelling and implication for thermobarometric estimates. *Contrib Mineral Petrol* 159:159–174
- Enrique P (1990) The Hercynian intrusive rocks of the Catalan Coastal Ranges (NE Spain). *Acta Geol Hisp* 25(1–2):39–64
- Evans JP, Chester FM (1995) Fluid-rock interaction in faults of the San Andreas system: Inferences from San Gabriel fault rock geochemistry and microstructures. *J Geophys Res* 100 (B7):13007–13020
- Fernández M, Banda E (1989) An approach to the thermal field in northeastern Spain. *Tectonophysics* 164:259–266
- Fournier RO (1991) The transition from hydrostatic to greater than hydrostatic fluid pressure in presently active continental hydrothermal systems in crystalline rocks. *Geophys Res Lett* 18(5):955–958
- Fujimoto K, Tanaka H, Higuchi T, Tomida N, Ohtani T, Ito H (2001) Alteration and mass transfer inferred from the Hirabayashi GSJ drill penetrating the Nojima Fault, Japan. *Isl Arc* 10:401–410
- Ganne J, De Andrade V, Weinberg R, Vidal O, Allibon J, Dubacq B, Baratoux L, Chardon D, Jessell M, Kagambega N, Naba S (2012) The dawn of modern earth plate subduction in the paleoproterozoic West African Craton (2.2–2.0 Ga). *Nat Geosci*. doi:10.1038/ngeo1321

- Gaspar-Escribano JM, Garcia-Castellanos D, Roca E, Cloetingh S (2004) Cenozoic vertical motions of the Catalan Coastal Ranges (NE Spain): the role of tectonics, isostasy, and surface transport. *Tectonics* 23:TC1004. doi:10.1029/2003TC001511
- Gil-Ibarguchi JI, Julivert M (1988) Petrología de la aureola metamórfica de la granodiorita de Barcelona en la Sierra de Collcerola (Tibidabo). *Est Geol* 44(5–6):353–374
- Gómez-Gras D, Ferrer C (1999) Caracterización petrológica de perfiles de meteorización antiguos desarrollados en granitos tardihercínicos de la Cordillera Costero Catalana. *Rev Soc Geol España* 12(2):281–299
- Grosch EG, Vidal O, Abu-Alam T, McLoughlin N (2012) *PT*-Constraints on the metamorphic evolution of the Paleoproterozoic Kromberg type-section, Barberton Greenstone Belt, South Africa. *J Petrol* 53(3):513–545
- Guimerà J (1984) Palaeogene evolution of deformation in the northeastern Iberian Peninsula. *Geol Mag* 121(5):413–420
- Haines SF, van der Pluijm BA (2012) Patterns of mineral transformation in clay gouge, with examples from low-angle normal fault rocks in the western USA. *J Struct Geol* 43:2–32
- Inoue A, Meunier A, Patrier-Mas P, Rigault C, Beaufort D, Vieillard Ph (2009) Application of chemical geothermometry to low-temperature trioctahedral chlorites. *Clays Clay Miner* 57(3):371–382
- Ivanov IP, Gurevich LP (1975) Experimental study of  $T$ - $X_{CO_2}$  boundaries of metamorphic zeolite facies. *Contrib Mineral Petrol* 53:55–60
- Jefferies SP, Holdsworth RE, Wibberley CAJ, Shimamoto T, Spiers CJ, Niemeijer AR, Lloyd GE (2006) The nature and importance of phyllonite development in crustal-scale fault cores: an example from the Median Tectonic Line, Japan. *J Struct Geol* 28:220–235
- Juez-Larré J (2003) Post late Paleozoic tectonothermal evolution of the northeastern margin of Iberia, assessed by fission-track and (U-Th)/He analyses. A case history from the Catalan Coastal Ranges. Dissertation, Vrije Universiteit
- Julivert M, Durán H (1990) Paleozoic stratigraphy of the Central and Northern part of the Catalanian Coastal Ranges (NE Spain). *Acta Geol Hisp* 25(1–2):3–12
- Kristmannsdóttir H, Tómasson J (1978) Zeolite zones in geothermal areas in Iceland. In: Sand LB, Mumpston FA (eds) *Natural Zeolites: occurrence, properties, Use*. Pergamon Press, Elmsford, NY, pp 277–284
- Lacroix B (2011) Interaction fluide-roche et comportement des phyllosilicates à basses températures en contexte sédimentaire: exemple du prisme orogénique sud-pyrénéen. Dissertation, Université de Franche Comté
- Lacroix B, Charpentier D, Buatier M, Vennemann T, Labaume P, Adatte T, Travé A, Dubois M (2012) Formation of chlorite during thrust fault reactivation. Record of fluid origin and P-T conditions in the Monte Perdido thrust fault (southern Pyrenees). *Contrib Mineral Petrol* 163(6):1083–1102
- Lanari P, Guillot S, Schwartz S, Vidal O, Tricart P, Riel N, Beyssac O (2012) Diachronous evolution of the alpine continental subduction wedge: evidence from P-T estimates in the Briançonnais Zone houillère (France-Western Alps). *J Geodyn* 56–57:39–54
- Leclère H, Buatier M, Charpentier D, Sizun JP, Labaume P, Cavailhes T (2012) Formation of phyllosilicates in a fault zone affecting deeply buried arkosic sandstones: their influence on petrophysical properties (Annot sandstones, French external Alps). *Swiss J Geosci* 105:299–312
- Liou JG, Seki Y, Guillemette RN, Sakai H (1985) Compositions and parageneses of secondary minerals in the Onikobe geothermal system, Japan. *Chem Geol* 49:1–20
- Ll Cabrerà (1981) Influencia de la tectónica en la sedimentación continental de la cuenca del Vallès-Penedès (provincia de Barcelona, España) durante el Mioceno inferior. *Acta Geol Hisp* 16(3):165–171
- López de Azcona JM (1983) Consideraciones sobre el grupo de manatiales de aguas mineromedicinales de Caldas de Montbui. In: *Monografía X Caldas de Montbui. Monografías de aguas mineromedicinales*, pp 5–21
- Martín-Martín JD, Tritlla J, Cardellach E, Gómez-Gras D (2006) Tectonically driven fluid flow and associated low-grade metamorphism during the Alpine compression in the eastern Iberian Chain (Spain). *J Geochem Explor* 89:267–270
- Martín-Martín JD, Salas R, Gómez-Gras D (2008) Datación por K-Ar de la diagénesis y el metamorfismo de muy bajo grado en red-beds permotriásicos de la Cadena Ibérica oriental (Castellón y Valencia): resultados preliminares. *Geo-Temas* 10:257–260
- Martín-Martín J, Salas R, Gómez-Gras D, Zwingmann H (2009) K/Ar isotopic dating of very low-grade metamorphic and diagenetic conditions during the Mesozoic rifting evolution of the Iberian Chain, Spain. XIV International Clay Conference, Italia
- Massone HJ, Schreyer W (1989) Stability field of the high-pressure assemblages talc-phengite and two new phengite barometers. *Eur J Mineral* 1:391–410
- Parra T, Vidal O, Agard P (2002) A thermodynamic model for Fe-Mg dioctahedral K White micas using data from phase-equilibrium experiments and natural pelitic assemblages. *Contrib Mineral Petrol* 143:706–732
- Piqué À, Canals À, Grandia F, Banks DA (2008) Mesozoic fluorite veins in NE Spain record regional base metal-rich brine circulation through basin and basement during extensional events. *Chem Geol* 257:139–152
- Roca E (1996) La evolución geodinámica de la Cuenca Catalano-Balear y áreas adyacentes desde el Mesozoico hasta la actualidad. *Acta Geol Hisp* 29:3–25
- Roca E, Guimerà J (1992) The Neogene structure of the eastern Iberian margin: structural constraints on the crustal evolution of the València trough (Western Mediterranean). *Tectonophysics* 203:203–218
- Roca E, Sans M, Cabrera L, Marzo M (1999) Oligocene to Middle Miocene evolution of the central Catalan margin (Northwestern Mediterranean). *Tectonophysics* 315:209–233
- Rossi C, Goldstein RH, Marfil R, Salas R, Benito MI, Permanyer A, de la Peña JA, Caja MA (2001) Diagenetic and oil migration history of the Kimmeridgian Ascla Formation, Maestrat Basin, Spain. *Mar Petrol Geol* 18:287–306
- Salas R, Casas A (1993) Mesozoic extensional tectonics, stratigraphy and crustal evolution during the Alpine cycle of the eastern Iberian basin. *Tectonophysics* 228(1–2):33–55
- Salas R, Guimerà J, Mas R, Martín-Closas C, Meléndez A, Alonso A (2001) Evolution of the Mesozoic central Iberian Rift System and its Cainozoic inversion (Iberian Chain). In: Ziegler PA, Cavazza W, Robertson AHF, Crasquin-Soleau S (eds) *Peri-Tethys Memoir 6: Peri-Tethyan Rift/Wrench Basins and Passive Margins*. *Mem Mus natn Hist Nat* 186:145–185
- Santanach P, Casas JM, Gratacós O, Liesa M, Muñoz JA, Sàbat F (2011) Variscan and Alpine structure of the hills of Barcelona: geology in an urban area. *J Iber Geol* 37(2):121–136
- Schwartz S, Tricart P, Guillot S, Lardeau JM, Vidal O (2009) Late tectonic and metamorphic evolution of the Piedmont accretionary wedge (Queyras Schistes lustrés, western Alps: evidences for tilting during Alpine collision. *Geol Soc Am Bull* 121:502–518
- Shelley D (1983) Igneous and metamorphic rocks under the microscope: classification, textures, microstructures and mineral preferred orientations. Chapman and Hall, London
- Sibson RH (2000) Fluid involvement in normal faulting. *J Geodyn* 29:469–499

- Sibson RH, Robert F, Poulsen KH (1988) High-angle reverse faults, fluid-pressure cycling, and mesothermal gold-quartz deposits. *Geology* 16:551–555
- ter Voorde M, Gaspar-Escribano JM, Juez-Larré J, Roca E, Cloetingh S (2007) Thermal effects of linked lithospheric and upper crustal-scale processes: Insights from numerical modeling of the Cenozoic Central Catalan Coastal Ranges (NE Spain). *Tectonics* 26:TC5018
- Trilla J (1974) Sobre el origen de las aguas termales de Caldes de Montbui. *Acta Geol Hisp IX* 4:144–148
- Tritlla J, Cardellach E (2003) Ba–Hg deposits in the Espadán ranges (Iberian Chain, Eastern Spain): an example of Cretaceous fluid circulation and Alpine overprinting. *J Geochem Explor* 78–79:579–584
- Vidal O, Parra T (2000) Exhumation of high pressure metapelites obtained from local equilibria for chlorite phengite assemblage. *Geol Mag* 35:139–161
- Vidal O, Parra T, Trotet F (2001) A thermodynamic model for Fe-Mg aluminous chlorite using data from phase equilibrium experiments and natural pelitic assemblages in the 100–600°C 1–25 kbar range. *Am J Sci* 63:557–592
- Vidal O, Parra T, Vieillard P (2005) Thermodynamic properties of the Tschermak solid solution in Fe-chlorite: application to natural examples and possible role of oxidation. *Am Mineral* 90:347–358
- Vidal O, De Andrade V, Lewin E, Munoz M, Parra T, Pascarelli S (2006) P-T-deformation-Fe<sup>3+</sup>/Fe<sup>2+</sup> mapping at the thin section scale and comparison with XANES mapping. Application to a garnet-bearing metapelite from the Sambagawa metamorphic belt (Japan). *J Metamorph Geol* 24:669–683
- Vidal O, Dubacq B, Lanari P (2010) Comment on “The role of H<sub>3</sub>O<sup>+</sup> in the crystal structure of illite” by F. Nieto, M. Melini, and I. Abad. *Clay Clay Miner* 58:717–720
- Vrolijk P, van der Pluijm BA (1999) Clay gouge. *J Struct Geol* 21(8–9):1039–1084
- Wintsch RP, Christoffersen R, Kronenberg AK (1995) Fluid-rock reaction weakening of fault zones. *J Geophys Res* 100 (B7):13021–13032